Title: ARID1A governs the silencing of sex-linked transcription during male meiosis in the mouse

Debashish U. Menon, Noel Murcia, & Terry Magnuson*

Department of Genetics, and Lineberger Comprehensive Cancer Center, The University of North Carolina at Chapel Hill, Chapel Hill, NC 27599-7264, USA

*Correspondence: trm4@med.unc.edu, Tel 919-357-2924, Fax 919-843-4682

Abstract

We present evidence implicating the BAF (BRG1/BRM Associated Factor) chromatin remodeler in meiotic sex chromosome inactivation (MSCI). By immunofluorescence (IF), the putative BAF DNA binding subunit, ARID1A (AT-rich Interaction Domain 1a), appeared enriched on the male sex chromosomes during diplonema of meiosis I. The germ cell-specific depletion of ARID1A resulted in a pachynema arrest and failure to repress sex-linked genes indicating a defective MSCI. Consistent with this defect, mutant sex chromosomes displayed an abnormal presence of elongating RNA polymerase II coupled with an overall increase in chromatin accessibility detectable by ATAC-seq. By investigating potential mechanisms underlying these anomalies, we identified a role for ARID1A in promoting the preferential enrichment of the histone variant, H3.3, on the sex chromosomes, a known hallmark of MSCI. Without ARID1A, the sex chromosomes appeared depleted of H3.3 at levels resembling autosomes. Higher resolution analyses by CUT&RUN revealed dramatic shifts in sex-linked H3.3 associations from discrete intergenic sites and broader gene-body domains to promoters in response to the loss of ARID1A. Several sex-linked sites displayed ectopic H3.3 occupancy that does not co-localize with DMC1 (DNA Meiotic Recombinase 1). This observation suggests a requirement for ARID1A in DMC1 localization to the asynapsed sex chromatids. We conclude that ARID1A-directed H3.3 localization influences sex chromosome gene regulation and DNA repair during meiosis I.

38 **Introduction**

39 Meiosis is central to the formation of haploid gametes from diploid pluripotent progenitors.
40 During meiosis, homologous chromosomes pair, exchange genetic material, align at the
41 metaphase plate and then segregate during the first meiotic cell division. Unlike autosomal
42 homologues, the X and Y chromosomes share limited homology. Unique mechanisms have
43 evolved to ensure these chromosomes are identified, sequestered, and processed in a parallel
44 but distinct process from autosomes.

45 XY chromosomes pair along the pseudo-autosomal region (PAR), leaving extensive regions of
46 the X and Y unpaired. These regions become enriched for DNA damage response (DDR)
47 factors, including ATR (Ataxia Telangiectasia and Rad3 related), TOPBP1 (DNA topoisomerase
48 II-binding protein 1), and MDC1 (Mediator of DNA Damage Checkpoint 1), which amplifies
49 γH2A.X across XY chromatin (Alavattam et al., 2021; ElInati et al., 2017; Fernandez-Capetillo et
50 al., 2003; Ichijima et al., 2011; Royo et al., 2013; Turner et al., 2004). XY chromatin acquires
51 further distinguishing features when canonical histones H3.1/3.2 are exchanged for variant H3.3
52 in that H3K9me3 (Histone lysine9 trimethylation) becomes elevated on XY chromatin relative to
53 autosomes (Hirota et al., 2018; van der Heijden et al., 2007; Yuen et al., 2014). As the XY
54 chromosomes become epigenetically distinct from autosomes, they also become physically
55 separated into a unique nuclear sub-compartment known as the XY body (Handel, 2004).
56 Transcriptional silencing of unpaired chromatin occurs during this phase of meiosis I, known as
57 meiotic silencing of unpaired chromatin, MSUC (Turner, 2007). MSUC of autosomal chromatin,
58 such as in response to an abnormal karyotype, causes pachynema arrest and cell death
59 (Baarends et al., 2005; Schimenti, 2005; Turner et al., 2005). However, silencing unpaired XY
60 chromatin results in a different outcome known as meiotic sex chromosome inactivation (MSCI)
61 (Alavattam et al., 2021). Sex chromosomes are required to undergo MSCI and become
62 transcriptionally inactivated. Failure to achieve MSCI triggers arrest and cell death (Ichijima et
63 al., 2012).

64 Chromatin factors that influence MSCI include the H3K9 methyltransferase, SETDB1 (SET
65 domain, bifurcated 1), PRC1 associated SCML2 (Sex comb on midleg-like protein 2), and testis-
66 specific reader of histone acetylation, BRDT (Bromodomain testis-specific protein) (Hasegawa
67 et al., 2015; Hirota et al., 2018; Manterola et al., 2018). Although our previous studies
68 demonstrated a critical requirement for SWI/SNF-directed transcriptional regulation during
69 meiosis, evidence for its involvement in MSCI is lacking (Menon et al., 2019). This lack of
70 evidence is also true for the PBAF (POLYBROMO1- BRG1/BRM Associated Factor) remodeler

71 within the SWI/SNF family, which we have shown is required for meiotic cell division (Menon et
72 al., 2021). Interestingly, the germ cell-specific depletion of the SWI/SNF catalytic subunit, BRG1
73 (Brahma-related gene-1), was shown to result in an early pachytene arrest (Kim et al., 2012).
74 Whether this suggests a role in MSCI remains an open question given that BRG1 associates
75 with both SWI/SNF remodelers, PBAF and BAF.

76 Here, we find that ARID1A (AT-rich Interaction Domain 1a), a BAF-specific putative DNA
77 binding subunit, is required for the transcriptional silencing of the sex chromosomes during
78 pachynema, thereby ensuring meiotic progression through prophase-I. Mechanistically, ARID1A
79 is necessary to establish MSCI hallmarks, such as the eviction of elongating RNA polymerase-II
80 (phosphorylated on Serine2 of carboxy-terminal domain; pSer2-RNAPII), limited sex-linked
81 chromatin accessibility, and hyper-accumulation of histone H3.3 on the sex body. Additionally,
82 ARID1A is required for the targeted localization of DMC1 to the unpaired sex chromatids,
83 implicating BAF-A-governed sex-linked chromatin dynamics in DNA repair.
84

85 **Results**
86
87 **Meiotic progression requires ARID1A**
88 Meiotic progression in male mice depends on SWI/SNF-regulated gene expression (Menon et
89 al., 2019; Menon et al., 2021). These studies raise the prospect of distinct SWI/SNF
90 subcomplexes governing stage-specific meiotic transcription (Menon et al., 2021). To
91 understand the meiotic functions of the biochemically distinct SWI/SNF BAF subcomplex, we
92 examined the spermatogenic expression profiles of the BAF subunits *Arid1a* and *Arid1b* using
93 single-cell RNA-seq data generated from testes (Ernst et al., 2019). *Arid1a* mRNA expression
94 occurred at various spermatogenic stages with notable expression at pachynema of meiotic
95 prophase I (Fig. S1A-C).

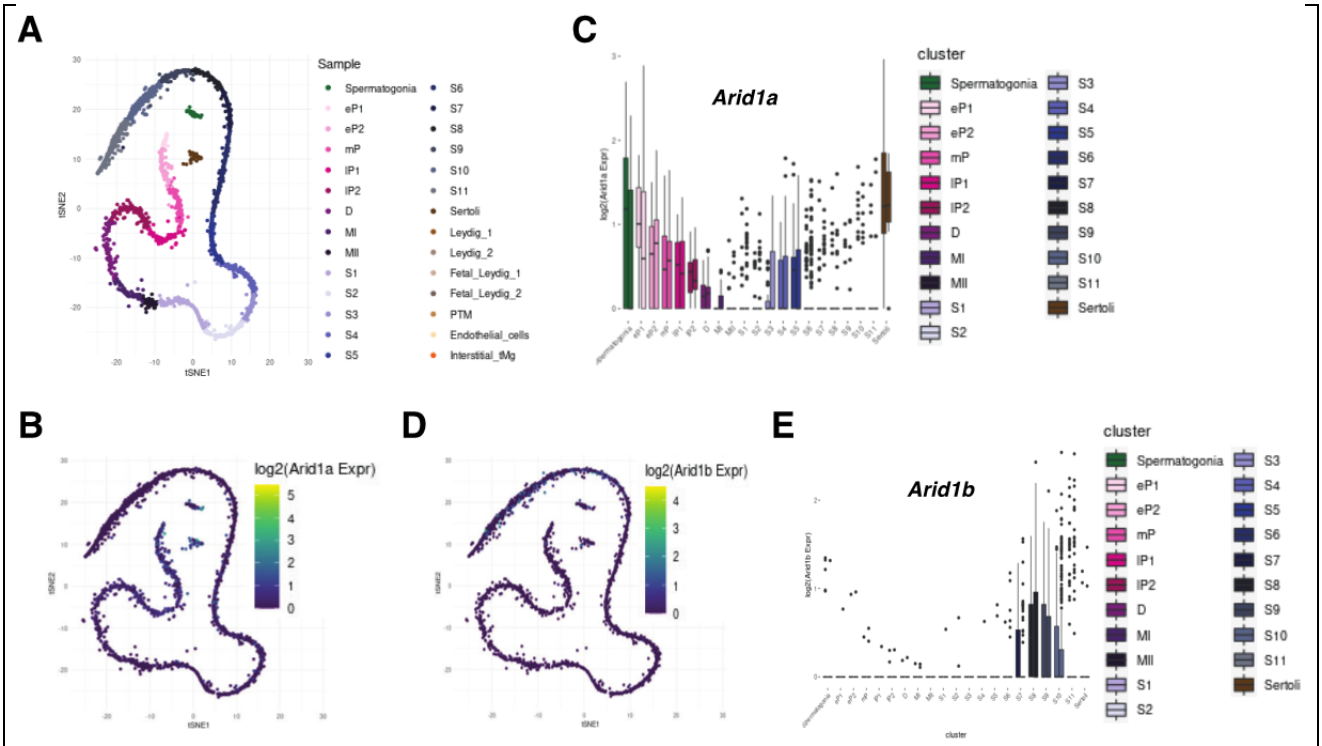

Figure S1. ARID1A transcripts detected in pachytene spermatocytes.
scRNA-seq profiles of *Arid1a* and *Arid1b* in adult testes from B6 mice (Ernst et al., 2019). (A) tSNE plot describing the clustering of various spermatogenic stages. LOG2 normalized expression counts of (B,C) *Arid1a* and (D,E) *Arid1b* represented by tSNE plots and bar plots. (B,D) tSNE plots illustrating the first (tSNE1, x-axis) and second dimensions (tSNE2, y-axis) . (C,E) Bar plots describe the gene's mRNA abundance (y-axis) across identified germ cell clusters (x-axis). (A) eP: early pachynema, mP: mid pachynema, lP: late pachynema, MI: Metaphase-I, MII: Metaphase-II, S1-S11: Spermatid stages. Plots generated with shiny app (https://marionilab.cruk.cam.ac.uk/SpermatoShiny)

Arid1b mRNA went undetectable until late in spermiogenesis (Fig. S1A, D-E). Consistent with its mRNA expression profile, pachytene spermatocytes featured abundant ARID1A protein, which was uniformly spread (Fig. 1). Late in diplonema, ARID1A appeared preferentially enriched on the sex chromosomes as compared to autosomes (Fig. 1). These data implicate ARID1A in meiotic sex chromosome inactivation (MSCI), a process essential for meiotic progression in males.

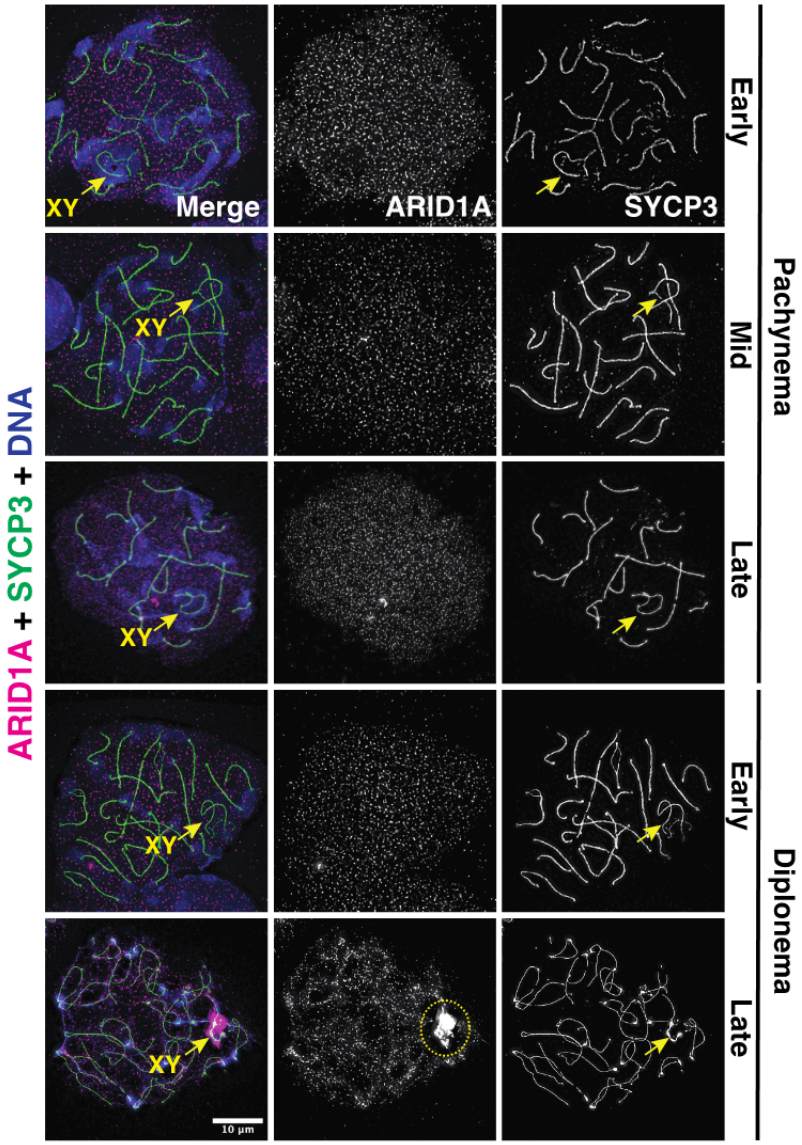

Fig 1. ARID1A associates with the sex body late in meiotic prophase-I.
Representative pachytene and diplotene spermatocyte spreads immunolabelled for ARID1A (magenta) and SYCP3 (green) and then counterstained for DNA (blue). Scale bar:10 µm, magnification: 100x.

To determine whether meiotic spermatocytes require ARID1A, we generated a germ cell-specific knock-out of *Arid1a* using the *Stra8-Cre* transgene expressed in spermatogonia (Sadate-Ngatchou et al., 2008). Contrary to our expectations, meiosis appeared unperturbed, as evidenced by seminiferous tubules featuring round and elongated spermatids in *Arid1a*^{cKO} testes (Fig. S2A). Furthermore, *Arid1a*^{cKO} epididymides featured mature spermatozoa, suggesting that mutants are capable of normal spermatogenesis (Fig. S2B). Although these data indicate that ARID1A is dispensable for spermatogenesis, we wanted to confirm that these results were not a technical artifact arising from inefficient *Stra8-Cre* mediated excision of the *Arid1a*^{fl} allele.

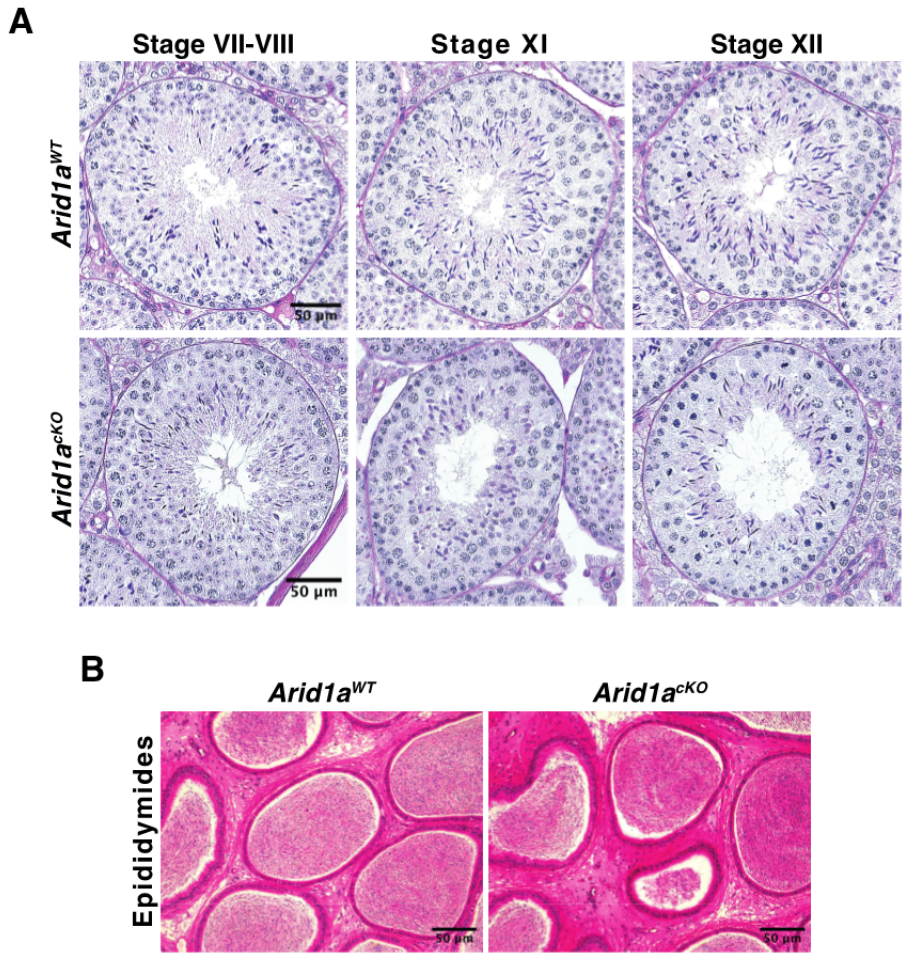

Fig S2. Spermatogenesis appears unperturbed in *Arid1a*^{cKO} males.
Histological examination of (A) PAS-stained seminiferous tubule sections and (B) H&E-stained cauda epididymal sections obtained from 10-week-old *Arid1a*^{WT} *and Arid1a*^{cKO} mice. The micrograph depicts seminiferous tubule staging and scale bars (50 µm). Magnification: 40x.

To address this question, we examined *Arid1a* transcripts isolated from *Arid1a*^{WT} and *Arid1a*^{cKO} Sta-Put purified populations of pachytene spermatocytes and round spermatids using RT-PCR (Fig. S3A). For cDNA synthesis, we used primers that amplify a 612 bp region spanning the *Arid1a* floxed exons 5 and 6. Assuming 100% CRE efficiency, we would expect to observe a 281 bp cDNA product associated with mRNA isolated from *Arid1a*^{cKO} spermatogenic cells. Instead, we observed cDNAs representative of the floxed (*fl*) allele and, to a greater extent, the excised (*Δ*) allele from mRNA isolated from *Arid1a*^{cKO} pachytene spermatocytes. These results indicated inefficient CRE activity (Fig. S3A). More importantly, the data suggest that a fraction of pachytene spermatocytes in *Arid1a*^{cKO} testes fail to undergo CRE-mediated excision resulting in escapers (internal controls). An examination of ARID1A levels in testes cryosections and meiotic spreads by immunofluorescence (IF) revealed a heterogenous population of pachytene

spermatocytes consisting of mutants lacking and internal controls expressing ARID1A (fig. S3B, C).

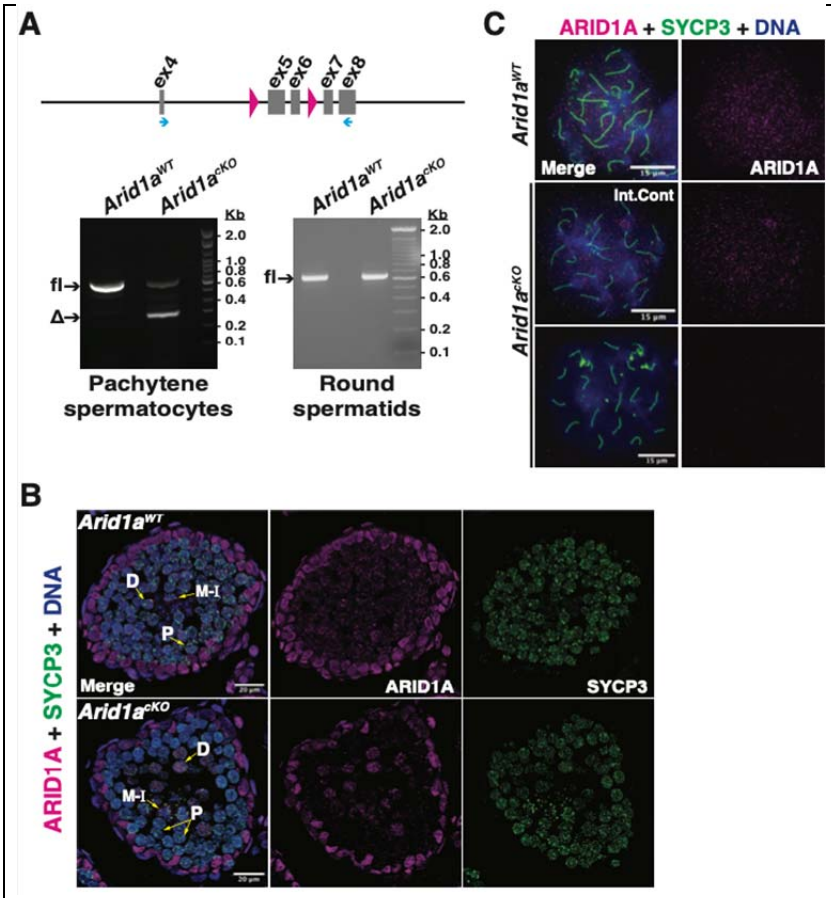

Fig S3. *Arid1a*^{cKO} testes display inefficient *Stra8-Cre* activity.
(A) Schematic (top) illustrating the region of *Arid1a*^{fl} allele spanning exons (ex) 4-8 (grey boxes) along with the location of *loxP* sites (solid magenta arrowheads) and primer annealing sites (blue arrows). (A bottom): analysis of the RT-PCR of *Arid1a* transcripts from STA-PUT purified populations of *Arid1a*^{WT} *and Arid1a*^{cKO} pachytene spermatocytes (left) and round spermatids (right). DNA electrophoresis gels indicate bands corresponding to the fl: floxed and Δ: excised PCR products. *Arid1a*^{WT} and *Arid1a*^{cKO} (B) testes cryosections, and (C) spermatocyte spreads, immunolabelled for ARID1A (magenta), SYCP3 (green), and counterstained for DNA (blue). (B) Scale bar: 20 μm, magnification: 63x, P: Pachytene, D: Diplotene, and M-I: Metaphase-I spermatocytes. (C) Scale bar:15 μm, magnification: 100x.

Furthermore, examining the meiotic profile associated with *Arid1a*^{cKO} revealed an accumulation of mutant spermatocytes (ARID1A^{-}) at mid-pachynema relative to *Arid1a*^{WT} spermatocyte spreads (Table 1). This result is indicative of a pachytene arrest. Although a few diplotene spermatocytes displaying a moderate reduction in ARID1A levels occurred in *Arid1a*^{cKO} relative to *Arid1a*^{WT} meiotic spreads (Table 1), mutant (ARID1A^{-}) diplotene and metaphase-I spermatocytes were undetectable in *Arid1a*^{cKO} testes (fig. S3B). It is possible that the pachytene spermatocytes that escape CRE activity progress to subsequent meiotic stages giving rise to genotypically normal gametes. All round spermatids isolated from *Arid1a*^{cKO} testes appeared only to express the normal transcript associated with the floxed allele (fig. S3A). Therefore, the perceived lack of a phenotype is an artifact of inefficient *Stra8-Cre* inefficiency. But more importantly, the data indicate that ARID1A is essential for progression beyond pachynema.

138

Meiotic Profile (P23)	*Arid1a*$^{fl/fl}$ (n= 166)	*Arid1a*^{cKO} (n= 124)
Pre-Lep/Leptonema	3.6 %	13.7 %
Zygonema	-	15.3 %
Early Pachynema	13.8 %	12.9 %
Mid Pachynema	22.89 %	40.3 %
late Pachynema	7.22 %	7.2 %
Early Diplonema	38.5 %	4.8 % *
Late Diplonema	14.45 %	5.6 % *

Table 1. The loss of ARID1A results in a pachytene arrest.
Table outlining the distribution of P23 *Arid1a*^{WT} and *Arid1a*^{cKO} meiotic prophase-I profiles. SYCP3 staining determined meiotic staging. Co-staining of ARID1A identified mutant spermatocytes from internal controls. The total number of spermatocytes scored included 166 for *Arida*$^{fl/fl}$ and 124 for *Arid1a*^{cKO}. * denotes *Arid1a*^{cKO} diplotene spermatocytes with partially reduced but not complete loss of ARID1A signal relative to controls.

139

140

141 **ARID1A regulates the transcriptional silencing of the sex chromosomes at pachynema**

142 The meiotic requirement of ARID1A and, more importantly, its association with the sex
143 chromosomes at diplonema prompted us to examine its role in MSCI. We hypothesized that
144 ARID1A might play a role in the transcriptional silencing of the sex-linked genes during meiosis.
145 To address this question, we performed RNA-seq on Sta-Put purified populations of pachytene
146 spermatocytes to profile changes in transcript abundance upon ARID1A deficiency. Differential
147 analysis of gene expression using DeSeq2 (Love et al., 2014) revealed an equal proportion of
148 significantly (FDR < 0.05) misexpressed genes displaying either elevated (up-regulated, n=
149 5824) or reduced (down-regulated, n=5821) transcript abundance in *Arid1a*^{cKO} relative to
150 *Arid1a*^{WT} pachytene spermatocytes (Fig. 2A). Notably, we detected significant misexpression of
151 53 % of all the sex-linked coding genes (593/1105) in response to an ARID1A deficiency.
152 Amongst these, 86.4% displayed elevated expression (n=512), whereas only 13.6% displayed
153 reduced (n=81) transcript abundance. This skew was even starker when only considering sex-
154 linked genes misexpressed by a magnitude of 2 LOG-fold or higher. Here, 97% (297/306) of the
155 misexpressed sex-linked genes displayed increased transcript abundance in response to an
156 ARID1A deficiency. Therefore, ARID1A predominantly affects the repression of sex-linked
157 genes during pachynema.

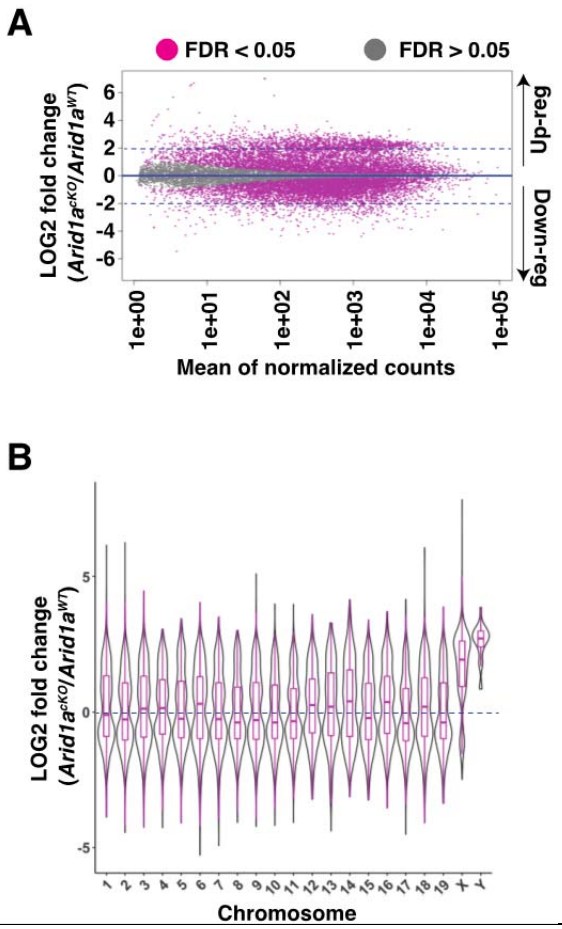

Fig 2. Requirement of ARID1A for the repression of sex-linked genes.
(A) MA plot describing the LOG2-fold-change (LFC, y-axis) in mean expression (x-axis) of genes displaying significant (FDR≤0.05, magenta dots) changes in *Arid1a*^{cKO} relative to *Arid1a*^{WT} pachytene spermatocytes. Dashed blue lines denote 2 LFC. Gray dots (FDR≥0.05) depict non-significant changes in gene expression. (B) Violin plot describing the LOG2-fold-change (LFC, y-axis) in the median chromosome-wide gene expression (x-axis) in *Arid1a*^{cKO} relative to *Arid1a*^{WT} pachytene spermatocytes. The dashed blue line denotes no change in gene expression.

An examination of changes in the average transcript abundance on a chromosome-wide basis showed that expression from the sex chromosomes was significantly higher than that from autosomes in response to the loss of ARID1A at pachynema (Fig. 2B). Therefore, ARID1A regulates the transcriptional repression of the sex chromosomes, implicating it in MSCI. Its predominant influence on sex-linked gene regulation may result from a preferential association of ARID1A with the sex chromosomes during meiosis. This association is undoubtedly the case late in diplonema. However, earlier in pachynema, when MSCI initiates, no sex chromosome-specific pattern of ARID1A enrichment was discernible, at least by IF (Fig. 1).

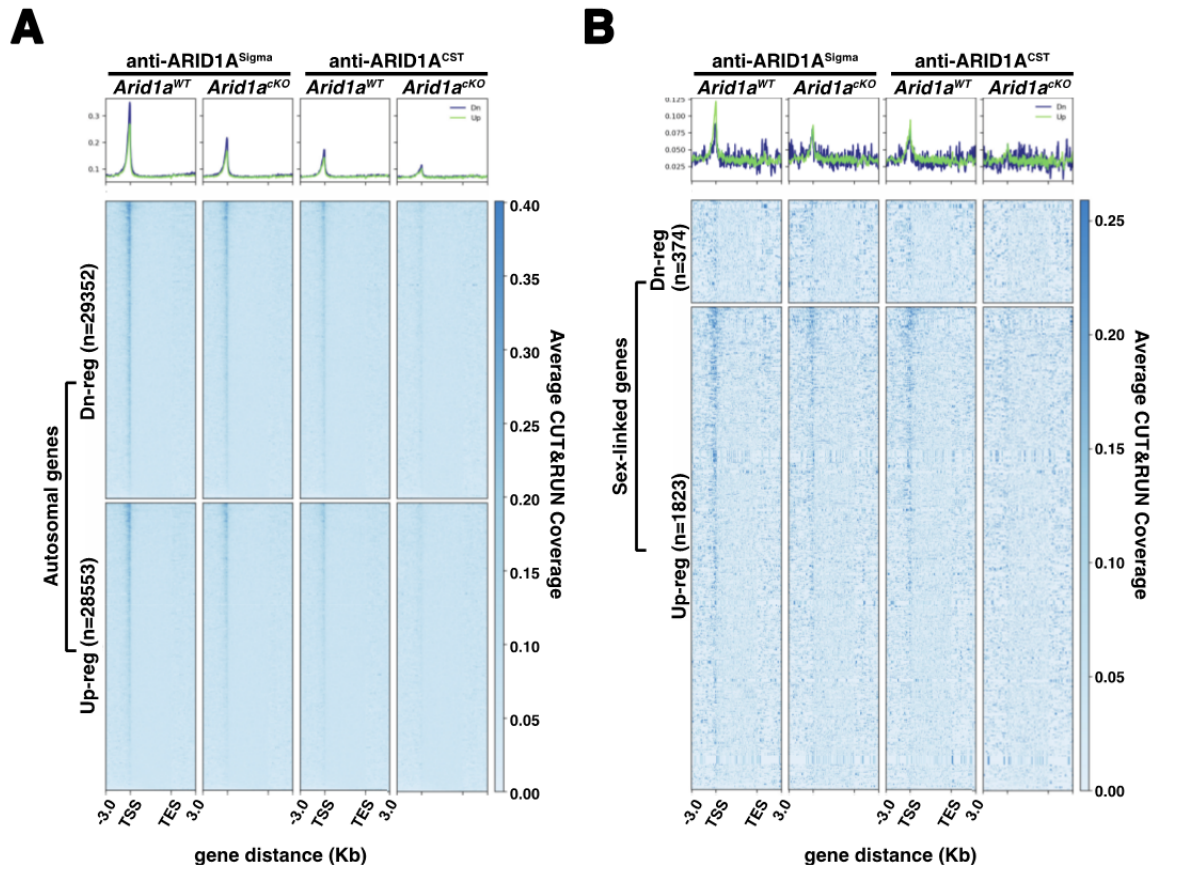

Fig S4. Transcription start sites of differentially expressed autosomal and sex-linked genes display ARID1A occupancy.
(A-B) Heatmap (bottom) and metaplot (top) displaying the average gene-wide enrichment of ARID1A associated with differentially expressed (A) autosomal and (B) sex-linked genes in *Arid1a*^{WT} and *Arid1a*^{cKO} pachytene spermatocytes. (A-B) The number of RefSeq annotations (n) associated with differentially regulated autosomal and sex-linked genes (rows) is indicated. Up-reg: misexpressed and Dn-reg: misrepressed genes in response to the loss of ARID1A. Average ARID1A CUT&RUN coverage was determined using two antibodies (anti-ARID1A^{Sigma}; anti-ARID1A^{CST}) plotted across RefSeq genes ± 3Kb.

We next determined ARID1A genomic localization at a higher resolution by CUT&RUN (Cleavage Under Targets & Release Using Nuclease) in pachytene spermatocytes. We detected ARID1A occupancy at promoters of differentially regulated target genes, irrespective of their chromosomal location, in *Arid1a*^{WT} relative to *Arid1a*^{cKO} (negative control) pachytene spermatocytes (Fig. S4). This result is consistent with the genome-wide distribution of ARID1A observed in pachytene spermatocyte spreads by IF (Fig. 1). Unnoticeable to IF, pachytene spermatocytes displayed a preferential association of ARID1A with promoters of normally repressed sex-linked genes, when detected by CUT&RUN (Fig. S4B), emphasizing its role in MSCI.

177

178 **ARID1A does not influence DNA damage response signaling on the sex body**

179 Unlike autosomal homologs that complete pairing during pachynema, the non-homologous
180 regions of the sex chromosomes feature unrepaired DNA double-strand breaks (DSBs). These
181 DNA DSBs recruit γH2Ax, a product of DNA damage response (DDR) signaling pathways
182 essential for establishing and maintaining MSCI (Turner, 2007). Therefore, to determine
183 whether ARID1A regulated MSCI by influencing DDR signaling, we first monitored the
184 association of γH2Ax with the sex chromosomes in response to the loss of ARID1A. By IF,
185 γH2Ax accumulation on the sex body appeared unperturbed in the mutant (ARID1A^{-}) relative to
186 internal controls (ARID1A^{+}) and *Arid1a*^{WT} pachytene spermatocytes (Fig. S5A). Consistent with
187 this, the recruitment of ATR (Ataxia Telangiectasia and Rad3 related), a kinase known to
188 phosphorylate γH2Ax and initiate MSCI (Turner et al., 2004; Royo et al., 2013), appeared
189 normal in the absence of ARID1A. These data indicate that sex-linked DDR signaling occurred
190 independently of ARID1A (Fig. S5B). Furthermore, MDC1 (Mediator of DNA damage
191 Checkpoint 1), a known γH2Ax reader that is essential for sex body formation (Ichijima et al.,
192 2011), remains robustly associated with the asynapsed sex chromosomes in the absence of
193 ARID1A during pachynema (Fig. S5C). These data show that the mechanisms underlying
194 ARID1A-mediated repression of the sex-linked transcription are mutually exclusive to DDR
195 pathways regulating sex body formation.

196

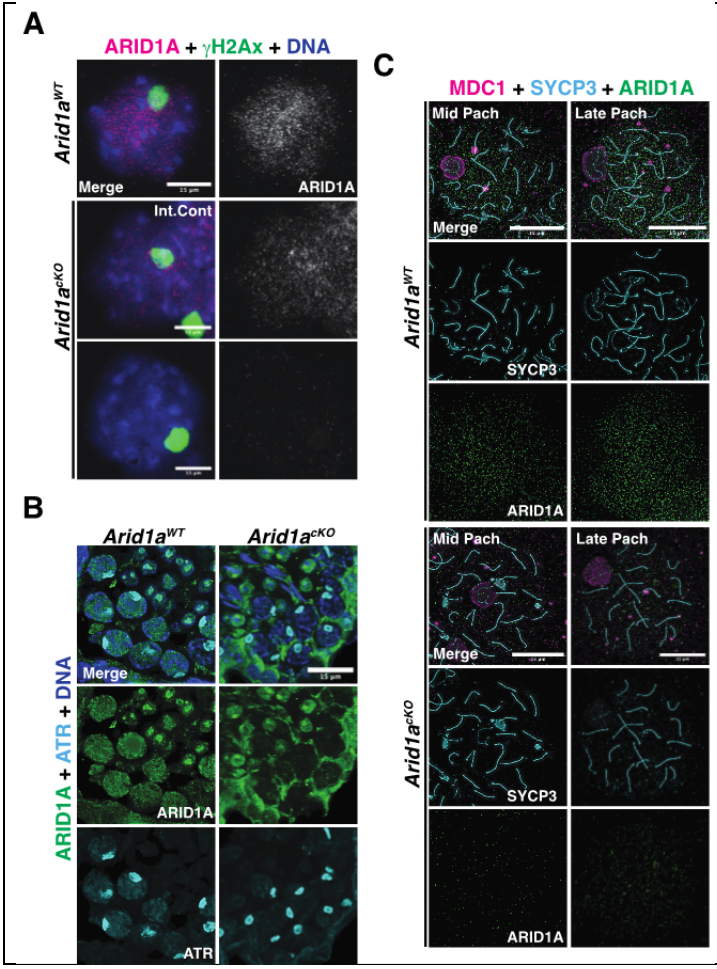

Fig S5. ARID1A does not influence sex body formation.
(A) *Arid1a*^{WT} and *Arid1a*^{cKO} spermatocyte spreads immunolabelled for ARID1A (magenta) and γH2Ax (green). Scale bar:15 µm, magnification: 100x. (B) Cross section of adult (3-month-old) *Arid1a*^{WT} and *Arid1a*^{cKO} seminiferous tubules immunolabelled for ARID1A (green) and ATR (cyan). Scale bar:15 µm, magnification: 63x. (C) *Arid1a*^{WT} and *Arid1a*^{cKO} pachytene spermatocytes immunolabelled for MDC1 (magenta), SYCP3 (cyan), and ARID1A (green). Scale bar:15 µm, magnification: 100x. (A-B) DNA counterstained with DAPI (blue).

ARID1A limits RNAPII localization to the sex chromosomes during pachynema

Apart from γH2Ax, the association of the sex chromosomes with RNA polymerase II (RNAPII) distinguishes the sex body from the autosomes during pachynema. Normally, pachytene spermatocytes display reduced levels of RNAPII on the sex body relative to autosomes (Khalil et al., 2004). This sub-nuclear localization of RNAPII coincides with increased transcriptional output, which peaks at diplonema (Ernst et al., 2019), underscoring the importance of targeted mechanisms regulating sex chromosome repression. Therefore, we were curious to test whether ARID1A influenced the nuclear localization of RNAPII during pachynema. We performed IF to monitor the localization of the actively transcribing (elongating) form of RNAPII marked by Serine2 phosphorylation (pSer2) on its carboxy-terminal domain (Noe Gonzalez et al., 2021). We monitored elongating RNAPII (pSer2) because its pausing regulates meiotic transcription (Alexander et al., 2022). By co-staining for RNAPII (pSer2) and SYCP3, we could stage pachynema and identify the sex chromosomes. While RNAPII (pSer2) localization to the autosomes appeared similar, we noticed increased levels of RNAPII (pSer2) association with

212 the sex chromosomes in *Arid1a*^{cKO} relative to *Arid1a*^{WT} mid and late pachytene spermatocytes
213 (Fig. 3A). By quantifying the RNAPII (pSer2) signal generated by IF, we detected a 1.5-fold
214 increase (p=0.0003) in the average RNAPII (pSer2) fluorescence associated with the sex
215 chromosomes in *Arid1a*^{cKO} relative to *Arid1a*^{WT} pachytene spermatocytes (Fig. 3B).

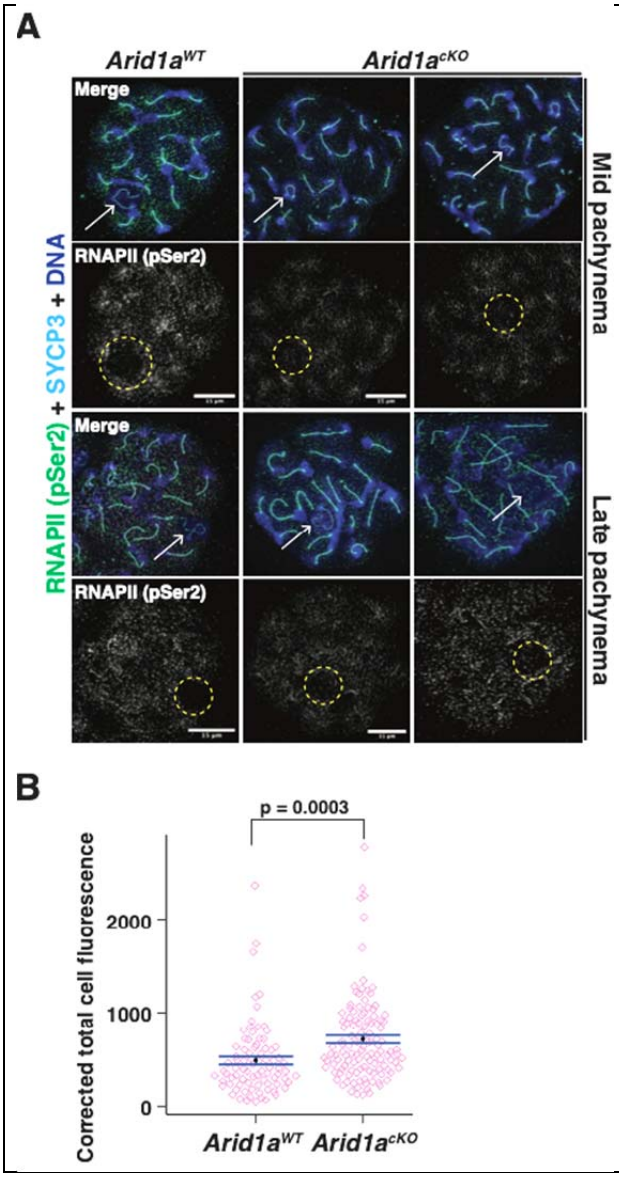

Fig 3. ARID1A limits RNA polymerase II (RNAPII) localization to the sex body. (A) *Arid1a*^{WT} and *Arid1a*^{cKO} pachytene spermatocytes immunolabelled for pSer2-RNAPII (green), SYCP3 (cyan), and counterstained with DAPI (blue). Scale bar:15 µm, magnification: 100x. The sex chromosomes (white arrow) and sex body (yellow dashed circle) are labeled. (B) Dot plot describing the corrected total pSer2-RNAPII fluorescence (y-axis) measured from *Arid1a*^{WT} (n = 82) and *Arid1a*^{cKO} (n= 119) pachytene spermatocytes (3 replicates per genotype). Empty diamonds (magenta) represent independent data points. Significance determined by a two-tailed unpaired Student's t-test p values. Data expressed as mean (black dot) ± SEM.

216

217 Due to technical difficulties, we could not simultaneously stain for ARID1A alongside SYCP3
218 and RNAPII (pSer2), making it impossible to distinguish internal controls from mutants in the
219 *Arid1a*^{cKO} meiotic spreads. This result suggests that the 1.5-fold increase in RNAPII association
220 with the sex body in *Arid1a*^{cKO} relative to *Arid1a*^{WT} pachytene spermatocytes is likely
221 underestimated. Therefore, our results indicate that ARID1A facilitates sex-linked gene

222 repression by limiting the association of elongating RNAPII with the sex chromosomes during
223 pachynema.
224
225 **ARID1A regulates promoter accessibility during pachynema**
226 Next, we hypothesized that ARID1A-governed chromatin remodeling might underlie its role in
227 limiting RNAPII accessibility on pachytene sex chromosomes. Therefore, we profiled changes in
228 chromatin accessibility in response to the loss of ARID1A using ATAC-seq. Normally, ATAC-seq
229 peaks (accessible chromatin) are mapped comparably across promoters (34%), intergenic
230 (22.8%), and intronic (21.5%) regions. In contrast, the loss of ARID1A resulted in a dramatic
231 shift towards predominantly promoter-associated ATAC-seq peaks with only a minority mapping
232 to intergenic and intronic regions (Fig .4A).
233 Consistent with an increase in the proportion of promoter-associated peaks, we detected an
234 increase in accessibility across transcription start sites (TSS) associated with both autosomal
235 and sex-linked DEG's in *Arid1a*^{cKO} relative to *Arid1a*^{WT} pachytene spermatocytes (Fig. 4B,C).
236 Furthermore, in the case of autosomal targets, chromatin accessibility at their TSSs was
237 enhanced irrespective of their transcriptional status, appearing indistinguishable between down-
238 regulated and up-regulated genes upon the loss of ARID1A (Fig. 4B). In contrast, on the sex
239 chromosomes, the loss of ARID1A seemed to have a prominent effect on TSS's associated with
240 up-regulated genes, which displayed greater chromatin accessibility relative to their down-
241 regulated counterparts (Fig. 4C). Therefore, the increased promoter accessibility of normally
242 repressed sex-linked genes may underlie their persistent transcription by RNAPII upon the loss
243 of ARID1A. Overall, these data highlight a role for BAF complexes in limiting promoter
244 accessibility, especially on the sex chromosomes during pachynema.

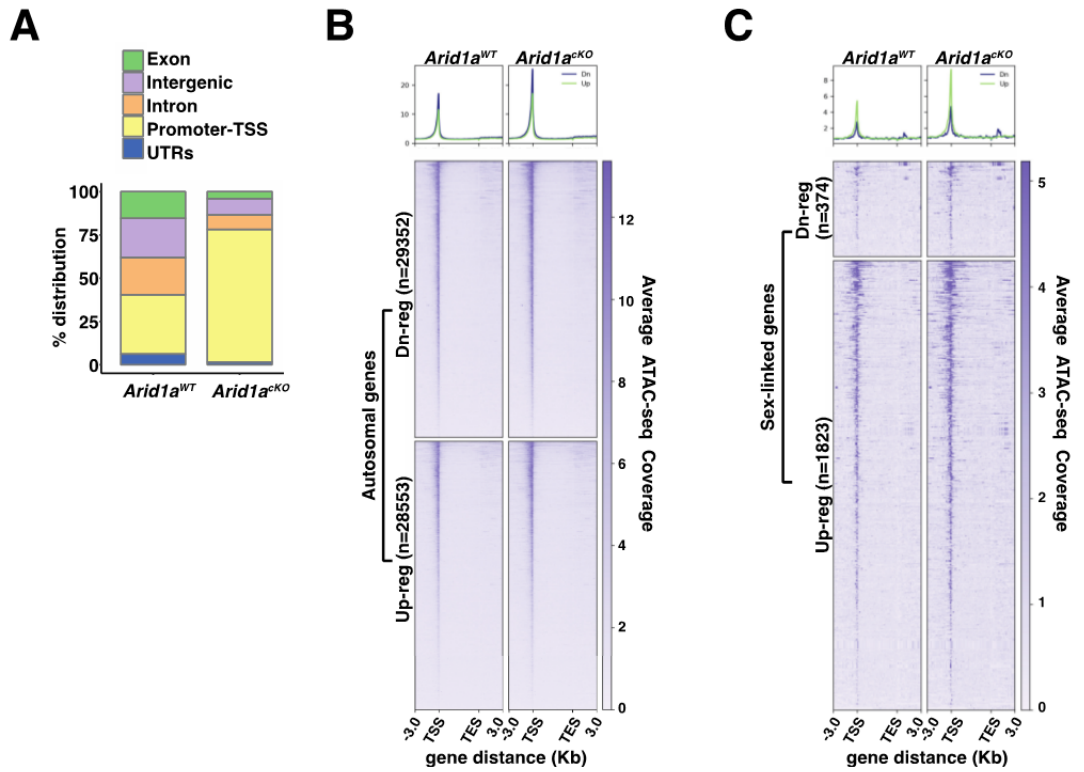

Fig 4. ARID1A limits promoter accessibility.
(A) Genomic associations of MACS2 derived ATAC-seq peak calls from *Arid1a*^{WT} and *Arid1a*^{cKO} pachytene spermatocytes. Percent (%) distribution of genomic annotations is indicated. (B-C) Heatmap (bottom) and metaplot (top) displaying the average ATAC-seq signal associated with differentially expressed (B) autosomal and (C) sex-linked genes in *Arid1a*^{WT} and *Arid1a*^{cKO} pachytene spermatocytes. (B-C) The number of RefSeq annotations (n) associated with differentially regulated genes (rows) is indicated. Up-reg: misexpressed, and Dn-reg: misrepressed genes in response to the loss of ARID1A. Average ATAC-seq coverage was plotted across RefSeq genes ± 3Kb.

245

246 **ARID1A regulates the chromatin composition of the sex body**

247 Chromatin remodelers regulate DNA accessibility by altering nucleosome positioning or
248 composition (Clapier et al., 2017). The latter outcome is interesting in the context of MSCI, given
249 that the sex body typically displays a striking enrichment of the variant histone H3.3 while
250 concomitantly appearing depleted of the canonical histones H3.1/3.2 (van der Heijden et al.,
251 2007; Yuen et al., 2014). Given that human ARID1A is known to regulate H3.3 genomic
252 associations (Reske et al., 2022), we tested whether a similar mechanism governed H3.3
253 localization to the sex chromosomes. To address this, we monitored H3.3 localization in
254 pachytene spermatocytes by IF, simultaneously staining for ARID1A and HORMAD1. The
255 former aided in mutant identification, while the latter labeled the pachytene sex chromosomes.
256 Consistent with previous reports, H3.3 can be seen preferentially coating the sex chromosomes
257 distinguishing it from autosomal chromatin during normal pachynema (Fig. 5A). Interestingly,

258 this sex body association of H3.3 was detected less frequently early in pachynema (17%),
259 becoming more pervasive during the mid (70 %) and late (95%) stages of pachynema. In
260 contrast, in the absence of ARID1A, H3.3 staining on the sex chromosomes was
261 indistinguishable from their autosomal counterparts throughout pachynema (Fig. 5A). Notably,

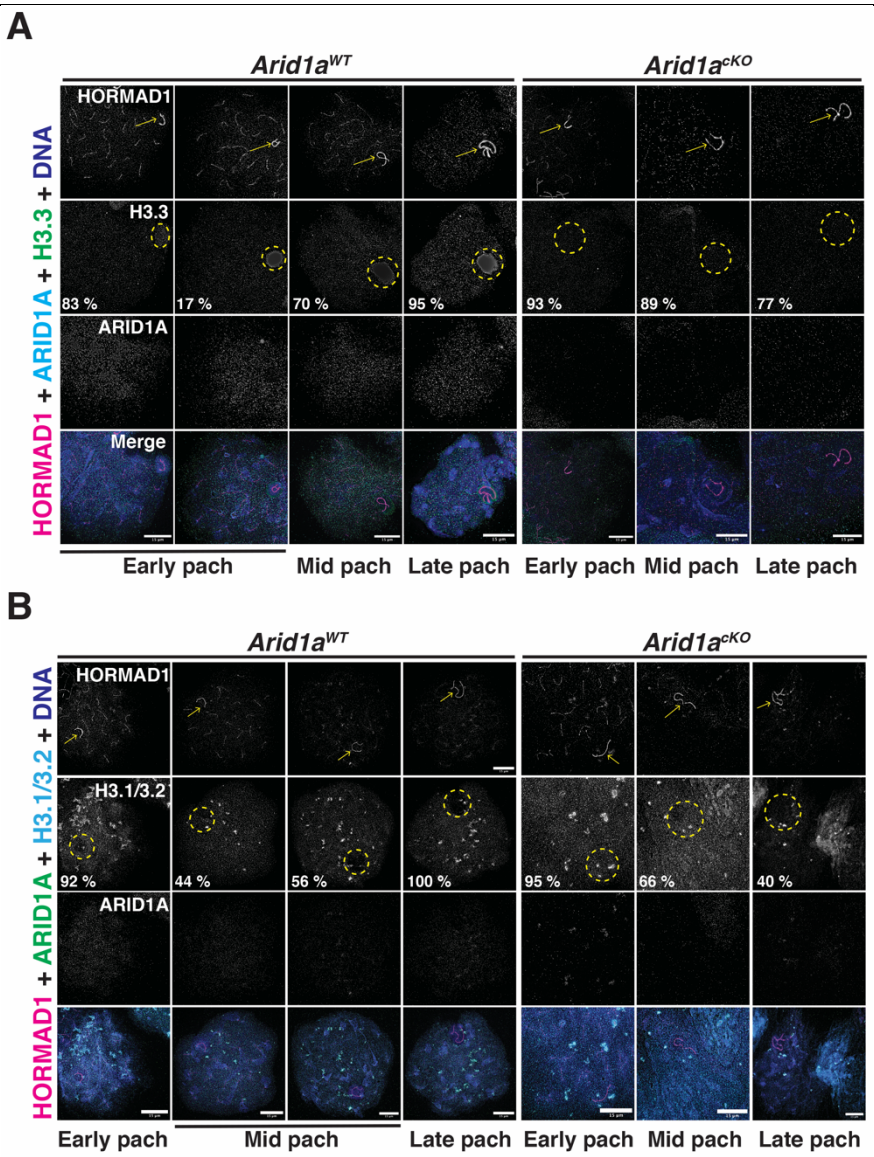

Fig 5. ARID1A influences the chromatin composition of the sex body. (A-B) *Arid1a*^{WT} and *Arid1a*^{cKO} pachytene spermatocytes immunolabelled for HORMAD1 (magenta), (A) ARID1A (cyan) and H3.3 (green), (B) ARID1A (green) and H3.1/3.2 (cyan). (A-B) Proportion (%) of *Arid1a*^{WT} and *Arid1a*^{cKO} early, mid, and late pachytene spermatocytes displaying distinct (A) H3.3, (B) H3.1/3.2 localization patterns with the sex body. For H3.3 immunostaining, the total number of *Arid1a*^{WT} pachytene spermatocytes: early = 144, mid= 274, late= 95; *Arid1a*^{cKO} pachytene spermatocytes: early = 43, mid= 86, late= 55, were scored, from 3 replicates each. For H3.1/3.2 immunostaining, the total number of *Arid1a*^{WT} pachytene spermatocytes: early = 91, mid= 124, late= 45; *Arid1a*^{cKO} pachytene spermatocytes: early = 22, mid= 116, late= 58, were scored, from 3 replicates each. DNA counterstained with DAPI (blue). The sex chromosomes (yellow arrow) and sex body (yellow dashed circle) are labeled. Scale bar:15 µm, magnification: 100x.

262 the majority of mutant mid (89%) and late (77%) pachytene spermatocytes lacked the typical
263 sex body enrichment of H3.3 (Fig. 5A), indicating that ARID1A dictates the preferential
264 accumulation of H3.3 on the sex body.

265
266 Next, we were curious to know the consequence of reduced H3.3 association on H3.1/3.2
267 occupancy on the sex body in response to the loss of ARID1A. We performed IF to monitor the
268 association of H3.1/3.2 with the sex chromosomes marked by HORMAD1 in response to the
269 loss of ARID1A. Like H3.3, canonical H3.1/3.2 appeared uniformly distributed genome-wide in
270 most early pachytene spermatocytes (92%). At the onset of pachynema, sex chromosomes
271 mostly displayed comparable H3.3 and H3.1/3.2 levels (Fig. 5A, B). However, this balance
272 changed during the subsequent sub-stages of pachynema. Although robust H3.3 levels
273 remained, H3.1/3.2 appeared excluded from the sex chromosomes in most mid (56%) and all
274 late pachytene spermatocytes (Fig. 5A, B). In contrast, the loss of ARID1A increased the
275 proportion of mid (66%) and late (40%) pachytene spermatocytes retaining H3.1/3.2 on sex-
276 linked chromatin (Fig. 5B). The abnormal retention of canonical H3.1/3.2 coincides with a lack of
277 H3.3 enrichment on sex-linked chromatin in response to the loss of ARID1A.
278
279 To determine whether these abnormal kinetics result from a genome-wide deficiency in H3.3,
280 we compared its levels by western blotting to find no difference in H3.3 abundance in *Arid1a*^{cKO}
281 relative to *Arid1a*^{WT} spermatocyte enriched populations (Fig. S6A). We also considered an
282 alternative possibility that ARID1A might promote the sex-linked enrichment of H3.3 by
283 influencing the expression of cognate chaperones like DAXX and HIRA during murine
284 pachynema (Rogers et al., 2004; van der Heijden et al., 2007). We addressed this by monitoring
285 DAXX and HIRA levels in response to the loss of ARID1A using IF. In the case of DAXX, we
286 examined meiotic spreads to find no changes in either the overall levels or sex chromosome
287 localization of DAXX in response to the loss of ARID1A (Fig. S6B). The same was also true of
288 HIRA, whose levels and nuclear localization in mutants appeared comparable to that seen in
289 internal (from *Arid1a*^{cKO}) and normal (*Arid1a*^{WT}) spermatocytes (Fig. S6C). Therefore, ARID1A
290 impacts H3.3 accumulation on the sex chromosomes without affecting its expression or
291 incorporation during pachynema. Overall, our data suggest that ARID1A influences MSCI by
292 regulating the composition of sex-linked chromatin.
293
294
295

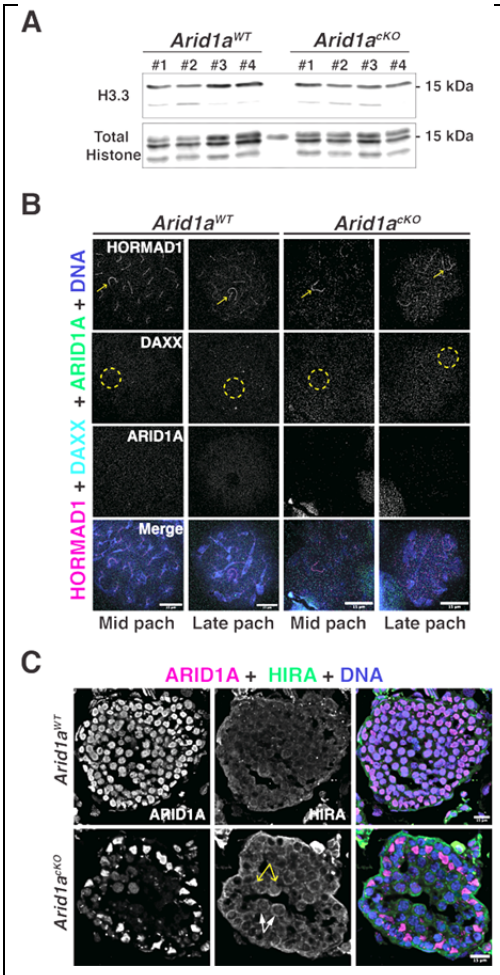

Fig S6. ARID1A does not influence the expression or incorporation of H3.3.
(A) Western blots on acid-extracted histones obtained from four independent replicates of P19 *Arid1a*^{WT} and *Arid1a*^{cKO} spermatogenic cells, displaying H3.3 abundance. Total histone levels from each sample are displayed. (B) *Arid1a*^{WT} and *Arid1a*^{cKO} pachytene spermatocytes immunolabelled for HORMAD1 (magenta), DAXX (cyan), and ARID1A (green). DNA counterstained with DAPI (blue). The sex chromosomes (yellow arrow) and sex body (yellow dashed circle) are labeled. Scale bar:15 µm, magnification: 100x. (C) *Arid1a*^{WT} and *Arid1a*^{cKO} testis cryosections immunolabelled for ARID1A (magenta) and HIRA (green). DNA counterstained with DAPI (blue). Representative mutant (white arrows) and internal control (yellow arrows) pachytene spermatocytes labeled in *Arid1a*^{cKO} testis cryosection. Scale bar: 15 µm, magnification: 63x.

ARID1A prevents the promoter accumulation of H3.3

To define the changes in the sex-linked associations of H3.3 at a higher resolution, we performed CUT&RUN on pachytene spermatocytes isolated from *Arid1a*^{WT} and *Arid1a*^{cKO} testes. Despite the appearance of a robust H3.3 IF signal from the sex body during normal pachynema (Fig. 5A), the Macs2 peak caller (Zhang et al., 2008) identified very few sex-linked peaks (n =224). These peaks were overwhelmingly associated with intergenic regions (Fig. S7A). Comparatively, a dramatically higher number of peaks (n=12183) primarily associated with genic (promoter, intron, and exon) regions occurred in *Arid1a*^{cKO} pachytene spermatocytes (Fig. S7A). More interestingly, there appeared to be a shift from few but overwhelmingly sex-linked H3.3 peaks (n=224; 98%) to autosomal H3.3 peaks (n=11512; 94.5 %) in response to the loss of ARID1A (Fig. S7A). Additionally, while the proportion of H3.3 sex-linked peaks in *Arid1a*^{cKO} pachytene spermatocytes were few (n=671; 5.5%), they outnumbered their *Arid1a*^{WT}

counterparts by 3-fold. These data suggest that the loss of ARID1A strongly influences H3.3 genomic associations.

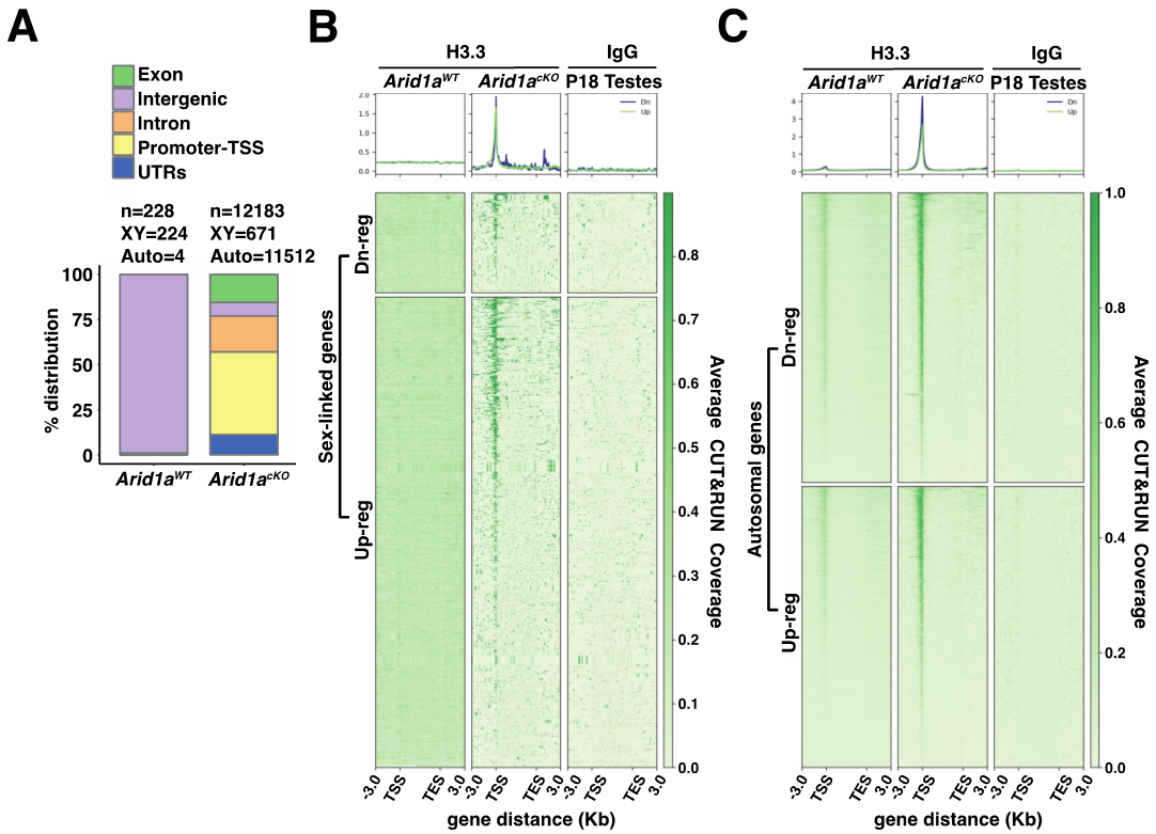

Fig S7. ARID1A limits H3.3 occupancy at promoters
(A) Genomic associations of MACS2 H3.3 peak calls from *Arid1a*^{WT} and *Arid1a*^{cKO} pachytene spermatocytes. Percent (%) distribution of genomic annotations is indicated. (B-C) Heatmap (bottom) and metaplot (top) displaying the average H3.3 signal associated with differentially expressed (B) sex-linked and (C) autosomal genes in *Arid1a*^{WT} and *Arid1a*^{cKO} pachytene spermatocytes. (B-C) The number of RefSeq annotations (n) associated with differentially regulated genes (rows) are indicated. Up-reg: misexpressed, and Dn-reg: misrepressed genes in response to the loss of ARID1A. Average H3.3 coverage plotted across RefSeq genes ± 3Kb.

Due to the increased representation of promoter-associated peaks in response to the loss of ARID1A, we monitored H3.3 association with TSSs of genes differentially regulated by ARID1A. Consistent with the genomic annotation of H3.3 peaks, we could not detect H3.3 enrichment at TSSs associated with ARID1A-regulated sex-linked genes relative to IgG control. H3.3 signal spread gene-wide in *Arid1a*^{WT} pachytene spermatocytes (Fig. S7B, Fig. S8A-top panel). In contrast, we observed a striking accumulation of H3.3 at the TSSs of sex-linked genes misexpressed without ARID1A (Fig. S7B, Fig. S8A). There is a transition from the gene-wide

320 spreading of H3.3 to promoter-proximal enrichment in response to the loss of ARID1A.
321 Concomitantly, X and Y-linked intergenic regions undergo a significant decrease in H3.3
322 occupancy upon ARID1A loss (Fig. S8A). A similar loss of H3.3 occupancy was also observed
323 at a handful of autosomal intergenic peaks (Fig. S7A, Fig. S8B - top).
324 Unlike the sex-linked targets, TSSs of ARID1A regulated autosomal genes displayed H3.3
325 enrichment relative to the IgG control (Fig. S7C, Fig. S8B - bottom). However, this TSS
326 occupancy appeared enhanced in *Arid1a*^{cKO} relative to *Arid1a*^{WT} pachytene spermatocytes (Fig.
327 S7C, Fig. S8B). Therefore, TSSs of both sex-linked and autosomal gene targets display
328 concordant changes in H3.3 occupancy. Overall, ARID1A occupancy at TSSs (Fig.S4) of
329 differentially regulated genes prevents the accumulation of H3.3 at target promoters.

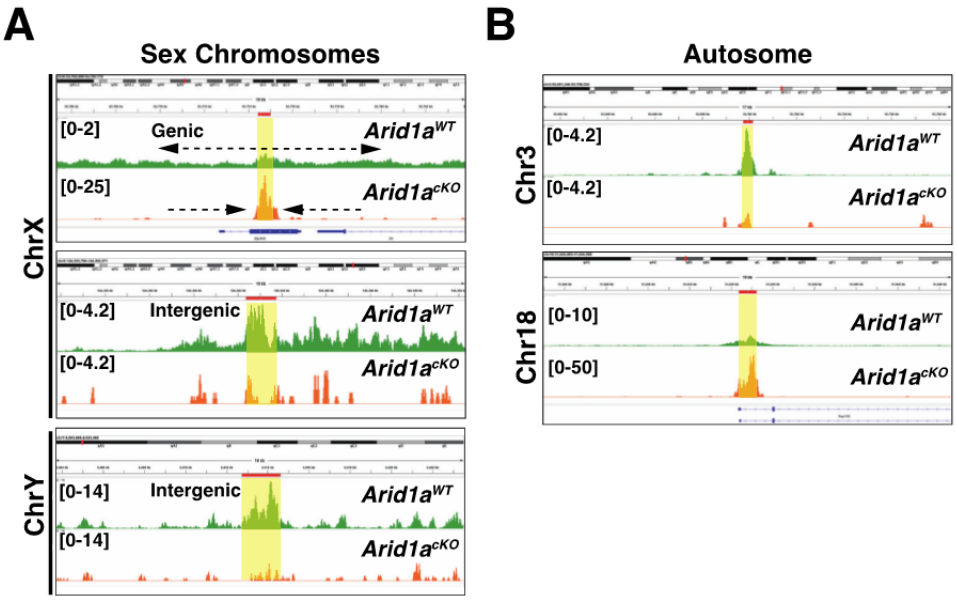

Fig S8. Genome browser views of ARID1A governed H3.3 genomic associations.
H3.3 CUT&RUN coverage from *Arid1a*^{WT} (green tracks) and *Arid1a*^{cKO} (Orange tracks) pachytene spermatocytes. Solid red bars and yellow highlights denote H3.3 peak calls (MACS2) from *Arid1a*^{WT} and *Arid1a*^{cKO} pachytene spermatocytes. Vertical viewing limits within parentheses.

330

331 **ARID1A restricts H3.3 occupancy to intergenic regions on the sex chromosomes**

332 Our analysis of the genome-wide localization of H3.3 in response to the loss of ARID1A would
333 argue that the abnormal increase in promoter-associated H3.3 results from its redistribution
334 from high-affinity sites (peaks) that are predominantly sex-linked and intergenic during normal
335 pachynema (Fig. S7A, Fig. S8). We focused our attention on these H3.3-occupied intergenic
336 sex-linked sites. Although the Macs2 algorithm identified only 224 sex-linked intergenic peaks,
337 we speculated that this approach filters out regions enriched for H3.3 that fail to meet the peak
338 calling threshold compounded by the pervasive spreading of H3.3 on the sex chromosomes

339 (Fig. 5A, Fig. S7B, S8A). We adopted an alternative strategy that involved identifying potential
340 H3.3 bound sites by monitoring their occupancy at ARID1A-governed accessible chromatin (Fig.
341 4A). We compared *Arid1a*^{WT} and *Arid1a*^{cKO} pachytene spermatocyte associated ATAC-seq
342 peaks to identify mutually exclusive and overlapping peaks using BEDTools (Quinlan and Hall,
343 2010). The resulting peaks could be categorized into lost (n=9), common (n=7194), or gained
344 (n=2246) based on their absence, persistence, or appearance, respectively, in *Arid1a*^{cKO} relative
345 to *Arid1a*^{WT} pachytene spermatocytes (Fig. 6A). Next, we examined the ATAC-seq signal at
346 these regions to find an increase in accessibility not only at gained peaks as expected but also
347 at common peaks in *Arid1a*^{cKO} relative to *Arid1a*^{WT} pachytene spermatocytes.

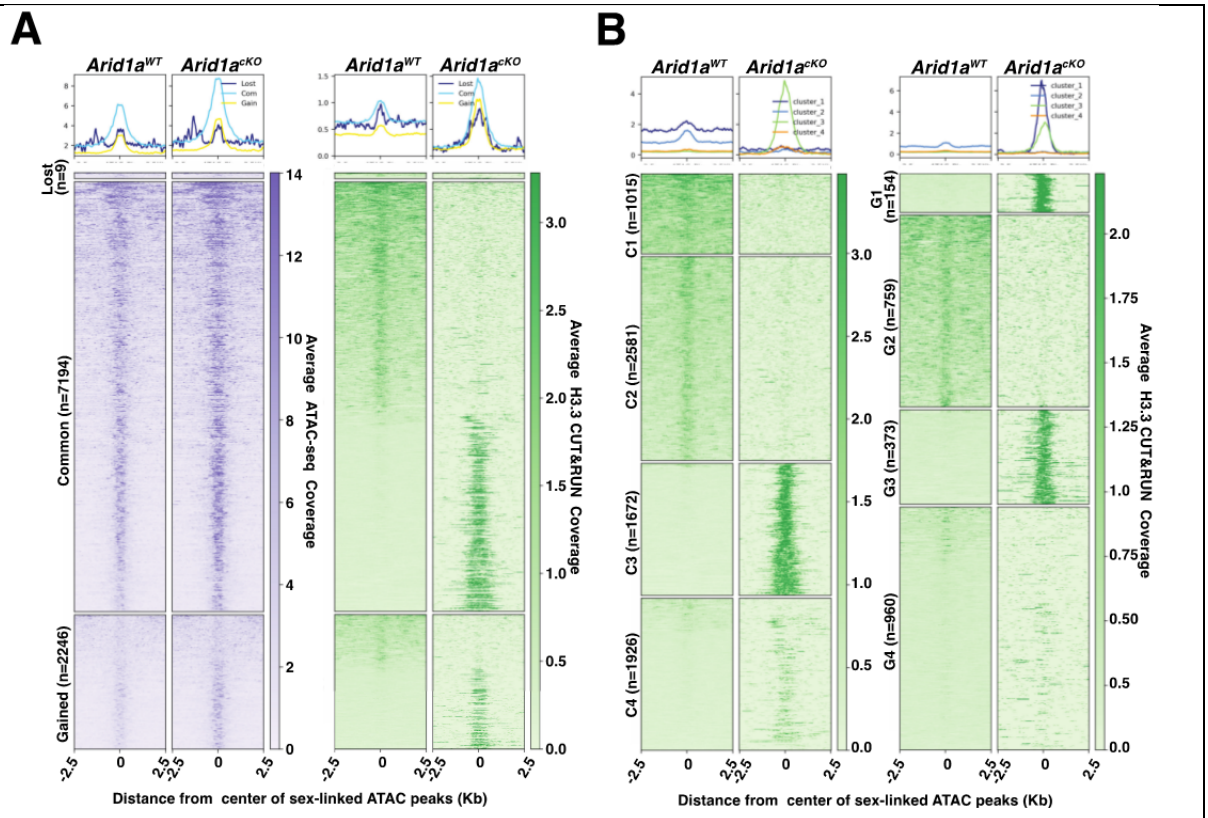

Fig 6. H3.3 displays differential occupancy across ARID1A governed sex-linked open chromatin. (A-B) Heatmaps (bottom) and metaplots (top) displaying average (A) chromatin accessibility (purple heatmap) and H3.3 enrichment (green heatmap) associated with lost, common, and gained ATAC-seq peak calls (MACS2), (B) enrichment of H3.3 at k-means clusters associated with common (C1-C4, left) and gained (G1-G4, right) ATAC-seq peaks, in *Arid1a*^{WT} and *Arid1a*^{cKO} pachytene spermatocytes. (A-B) ATAC-seq and H3.3 coverage plotted over a 5 Kb window centered at ATAC-seq peaks (MACS2). Number of ATAC-seq peak calls (n) associated with each category is indicated.

348

349 Despite being labeled as lost, these regions did not display the expected loss in ATAC-seq
350 signal in *Arid1a*^{cKO} relative to *Arid1a*^{WT} pachytene spermatocytes (Fig. 6A, left panel). The ATAC

351 signal appears unchanged, highlighting the possibility that lost regions were labeled as such
352 because they failed to satisfy Macs2 peak thresholds in *Arid1a*^{cKO} pachytene spermatocytes,
353 especially given the comparatively higher magnitude of ATAC signal surrounding the common
354 and gained peaks (Fig. 6A, left panel). We restricted our analysis to common and gained sites
355 constituting 99 % of sex-linked regions subject to ARID1A-regulated chromatin accessibility.
356 By plotting the average H3.3 coverage at sites associated with common and gained peaks, we
357 detected striking differences in H3.3 occupancy. Briefly, both common and gained open
358 chromatin regions consisted of loci differentiated by either a loss or robust increase in H3.3
359 occupancy in *Arid1a*^{cKO} relative to *Arid1a*^{WT} pachytene spermatocytes (Fig. 6A, left panel). To
360 gain further insight, we performed k-means clustering, based on H3.3 occupancy, to identify 4
361 clusters associated with either common (C1-C4) or gained (G1-G4) peaks (Fig. 6B). The
362 clusters associated with common ATAC-seq peaks displayed contrasting changes in H3.3
363 occupancy in response to the loss of ARID1A. C1 and C2 represented regions deficient for
364 H3.3, while C3 and C4 represent regions that gained H3.3 binding in *Arid1a*^{cKO} relative to
365 *Arid1a*^{WT} pachytene spermatocytes (Fig. 6B, left panel). Similarly, clusters associated with
366 gained ATAC-seq peaks, namely, G1 and G3, represented sites that gained H3.3 occupancy,
367 while G2 identified sites that lost H3.3 occupancy. We also noticed a gain in H3.3 binding at
368 regions associated with G4 in response to the loss of ARID1A, albeit at significantly reduced
369 coverage relative to G1 and G2 (Fig. 6B, right panel). Genomic annotations of common and
370 gained k-means clusters revealed that the sites that displayed a loss of H3.3 binding
371 (represented by C1 + C2, G2) in response to the loss of ARID1A were intergenic (Fig. S9A).
372
373 In contrast, those that gained H3.3 localization (represented by C3, C4, G1+G3, and G4)
374 distributed differentially between intergenic and genic regions (Fig. S9A). Therefore, these data
375 support our idea that ARID1A restricts H3.3 occupancy primarily to intergenic sites on the sex
376 chromosomes. Furthermore, the loss of ARID1A triggers an abnormal redistribution of H3.3 to
377 genic regions. Therefore, the increased promoter occupancy of H3.3 is an indirect consequence
378 of ARID1A loss.
379

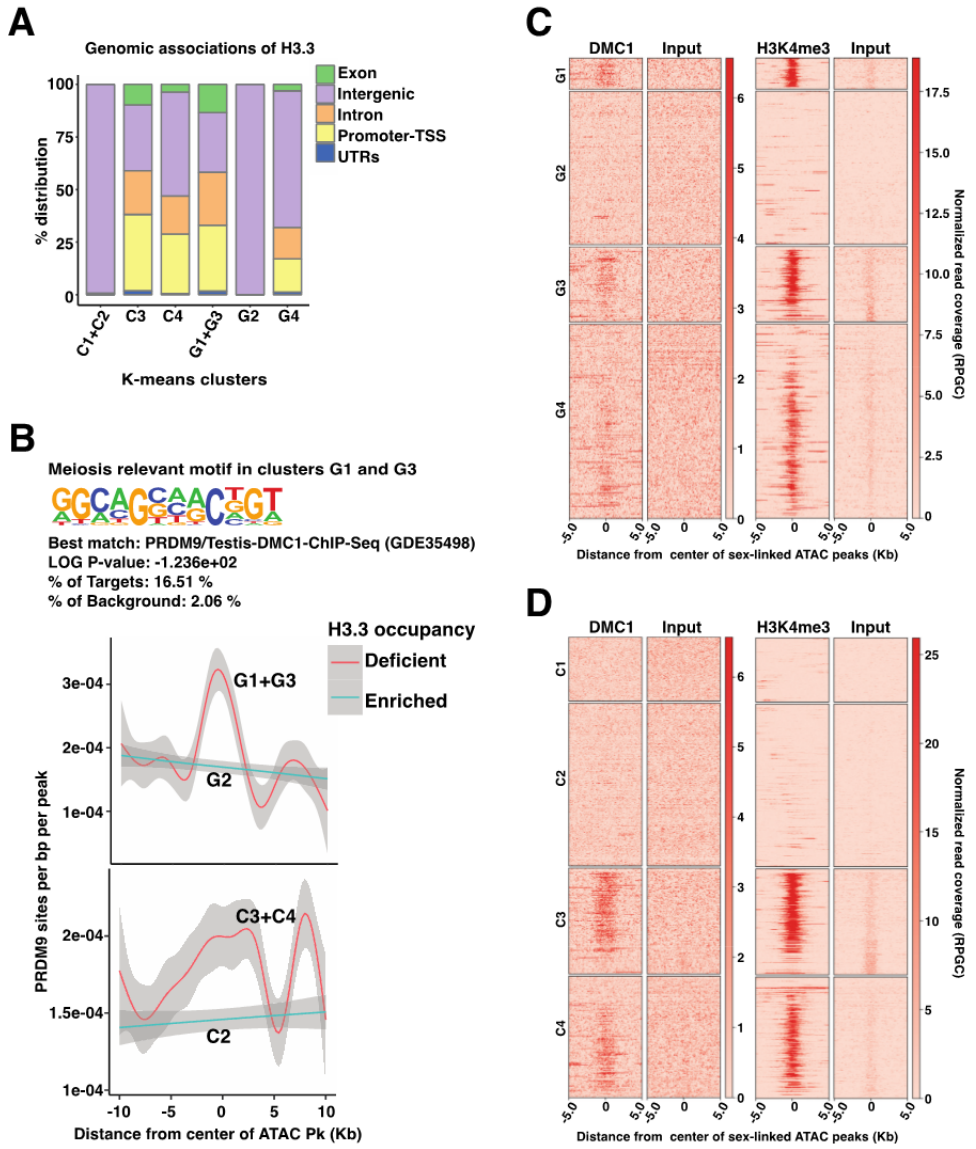

Fig S9. H3.3 occupancy is antagonistic to DMC1 associations in non-homologous sex-linked regions. (A) Genomic associations of common (C1-C4) and gained (G1-G4) k-means clusters in pachytene spermatocytes. Percent (%) distribution of genomic annotations is indicated. (B) Results of PRDM9 motif enrichment analyses at gained (G1 and G3), k-means clusters (top), and plots describing the frequency of PRDM9 motifs (y-axis) spanning a 5 Kb window centered at ATAC-seq peaks (x-axis) associated with gained (middle) and common (bottom) k-means clusters that are either deficient (orange trend line) or enriched (cyan trend line) for H3.3 occupancy. Trend lines were generated using generalized additive mode smoothing (gam). 95% confidence intervals (gray shading) are indicated. (C-D) Heatmaps displaying testes DMC1 (left) and pachytene spermatocyte associated H3K4me3 (right) enrichment relative to input at k-means clusters associated with (C) gained (G1-G4), and (D) common (C1-C4) ATAC-seq peaks. (C-D) DMC1 and H3K4me3 coverage plotted over a 10 Kb window centered at ATAC-seq peaks (MACS2).

380

381

382 **ARID1A-governed H3.3 localization influences the sex-linked association of DMC1**

383 To gain further insight into the mechanisms regulating H3.3 associations on the sex
384 chromosomes, we examined the regions associated with various k-means clusters to
385 investigate the enrichment of relevant motifs. To our surprise, we detected an enrichment of the
386 motif associated with the DSB hotspot specifier, PRDM9 (PR domain-containing protein 9), in
387 clusters related to gained peaks, G1 and G3 (Fig . S9B, top). Additionally, we observed an
388 increased frequency of PRDM9 motif centered at gained ATAC-seq peaks associated with G1
389 and G3 (Fig . S9B, middle).

390

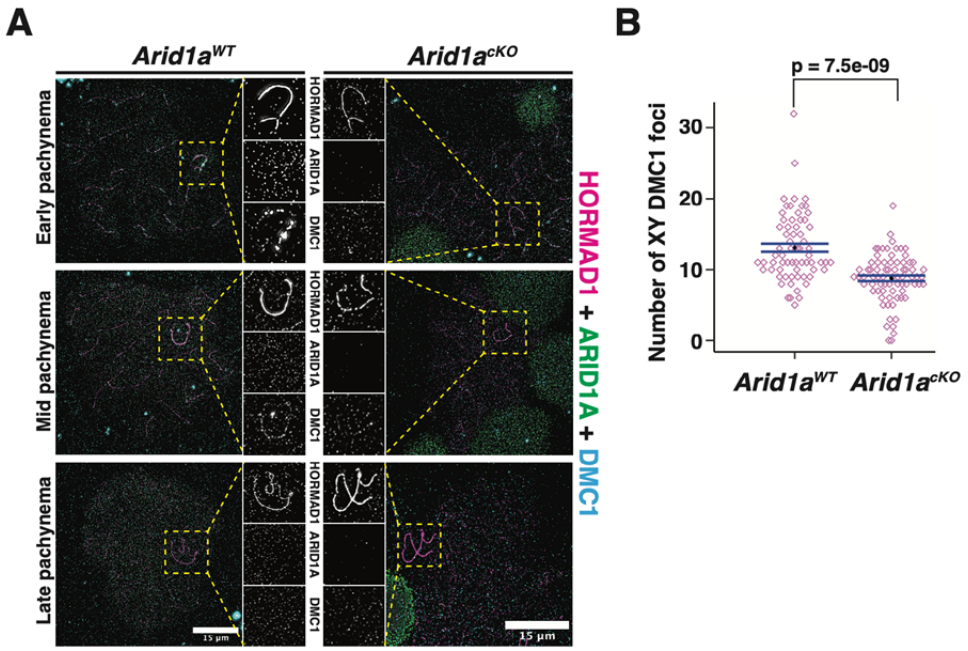

Fig 7. ARID1A influences the axial association of DMC1 with the XY during pachynema. (A) *Arid1a*^{WT} and *Arid1a*^{cKO} pachytene spermatocytes immunolabelled for HORMAD1 (magenta), ARID1A (green), DMC1 (cyan), and counterstained with DAPI (blue). Scale bar:15 µm, magnification: 100x. A magnified view of the sex chromosomes is indicated (yellow dashed square). (B) Dot plot displaying the number of sex-linked DMC1 foci (y-axis) quantified from *Arid1a*^{WT} (n = 66) and *Arid1a*^{cKO} (ARID1A^{-}, n= 75) pachytene spermatocytes, obtained from 3 replicates each. Empty diamonds (magenta) represent independent data points. Significance determined using a two-tailed unpaired Student's t-test p values. Data expressed as mean (black dot) ± SEM.

391

392 Interestingly, regions associated with G1 and G3 usually are devoid of H3.3 (Fig. 6B), implying a
393 potential antagonism between H3.3 occupancy and the occurrence of meiotic DNA DSBs.
394 Gained ATAC-seq peaks associated with G2, which usually displays H3.3 occupancy, appeared
395 devoid of PRDM9 motif occurrences relative to G1 and G3 (Fig. S9B, middle). Next, we

396 determined the frequency of the PRDM9 motif at k-means clusters associated with common
397 ATAC-seq peaks. These regions also displayed a dichotomous association with H3.3 (Fig. 6B).
398 C3 and C4, usually deficient in H3.3, showed an increased frequency of PRDM9 motifs relative
399 to C2, which typically displays H3.3 binding (Fig. S9B, bottom). These data confirm an
400 antagonistic relationship between H3.3 and meiotic DNA DSBs.
401

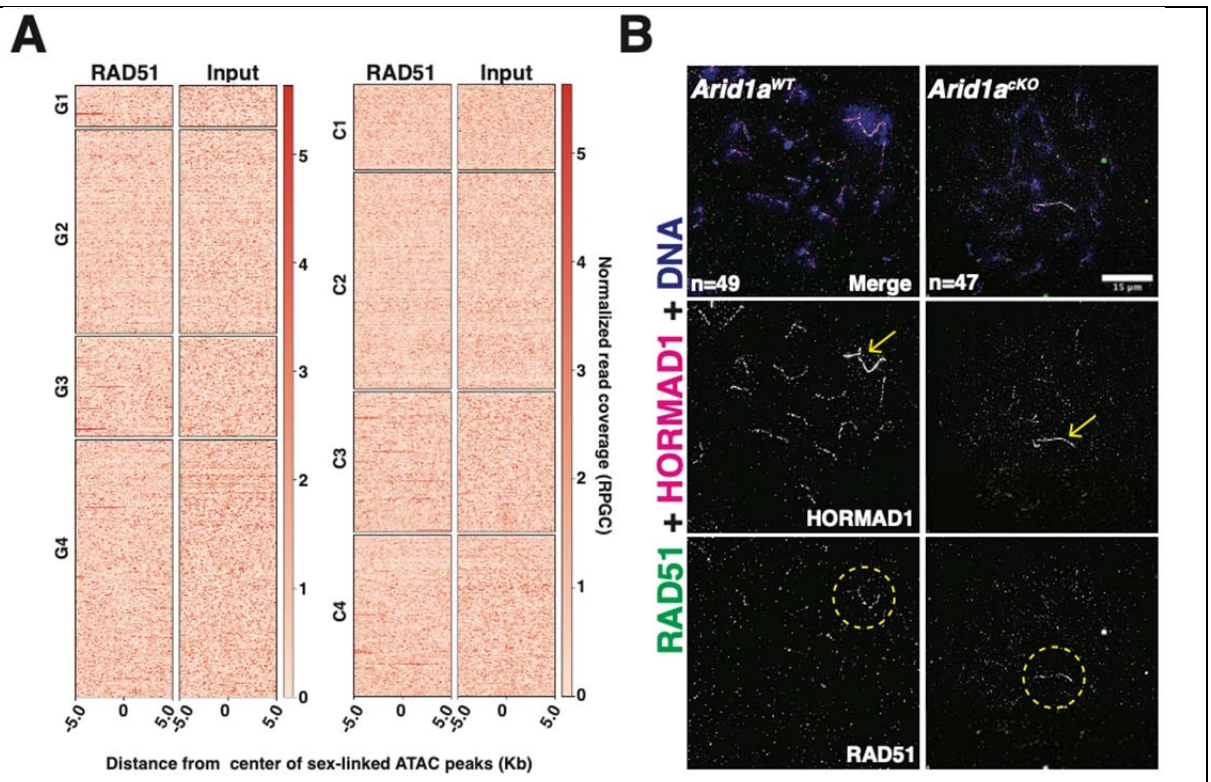

Fig S10. ARID1A does not affect the axial association of RAD51 with the XY during pachynema. (A) Heatmaps displaying testes RAD51 enrichment relative to input at k-means clusters associated with gained (G1-G4, left) and common (C1-C4, right) ATAC-seq peaks. RAD51 coverage plotted over a 10 Kb window centered at ATAC-seq peaks (MACS2). (B) *Arid1a*^{WT} and *Arid1a*^{cKO} pachytene spermatocytes immunolabelled for HORMAD1 (magenta), RAD51 (green) and counterstained with DAPI (blue). Scale bar:15 μm, magnification: 100x. Yellow arrows and dashed circles label the sex chromosomes.

402

403 Since the PRDM9 motifs identified from SSDS (Single-Stranded DNA Seq) data were generated
404 to map the genomic associations of DNA repair factor DMC1(Brick et al., 2012), we monitored
405 its enrichment at the various k-means clusters. We also monitored the association of markers of
406 meiotic DNA DSBs, such as the PRDM9 catalyzed H3K4me3 at common and gained k-means
407 clusters using published ChIP-seq data from pachytene spermatocytes (Maezawa et al.,
408 2018a). Consistent with the motif analyses, DMC1 occupancy and H3K4me3 enrichment

occurred at gained and common ATAC-seq peaks associated with k-means clusters, normally devoid of H3.3, namely, G1, G3, G4, C3, and C4 (Fig. S9C, D).

These data suggest that ARID1A might indirectly influence DNA DSB repair on the sex chromosomes by regulating the localization of H3.3. To test this conclusion, we monitored the association of DMC1 on the sex chromosomes, in response to the loss of ARID1A, by IF. Normally, DMC1 foci appear distributed along the non-homologous arms of the X and Y chromosomes from early to mid-pachynema, only disappearing by late pachynema (Fig. 7A, left, panel insets) (Moens et al., 2002). In contrast, in the absence of ARID1A, we observed a marked reduction in the number of DMC1 foci (Fig. 7A, right, panel insets). Quantification of DMC1 foci in Arid1a^{cKO} relative to Arid1a^{WT} pachytene spermatocytes revealed a significant decrease in the sex-linked association of DMC1 in the absence of ARID1A (Fig. 7B). Along with DMC1, the mitotic DNA recombinase, RAD51, is also known to localize to the non-homologous arms of the sex chromosomes (Moens et al., 1997; Moens et al., 2002). Therefore, we determined whether ARID1A also influenced the sex-linked association of RAD51. First, we analyzed previously generated RAD51-SSDS data (Hinch et al., 2020) to monitor its enrichment across the various k-means clusters associated with common and gained ATAC-seq peaks. Unlike DMC1, we found no detectable levels of RAD51 at any k-means clusters (Fig. S10A). Furthermore, the formation of RAD51 foci along the asynapsed axes of the sex chromosomes appeared unchanged in *Arid1a*^{cKO} relative to *Arid1a*^{WT} pachytene spermatocytes (Fig. S10B). Therefore, ARID1A is necessary for the normal sex-linked association of DMC1 but not RAD51. More importantly, our data highlight a dual role for ARID1A in regulating sex chromosome repression and DNA repair (Fig. 8).

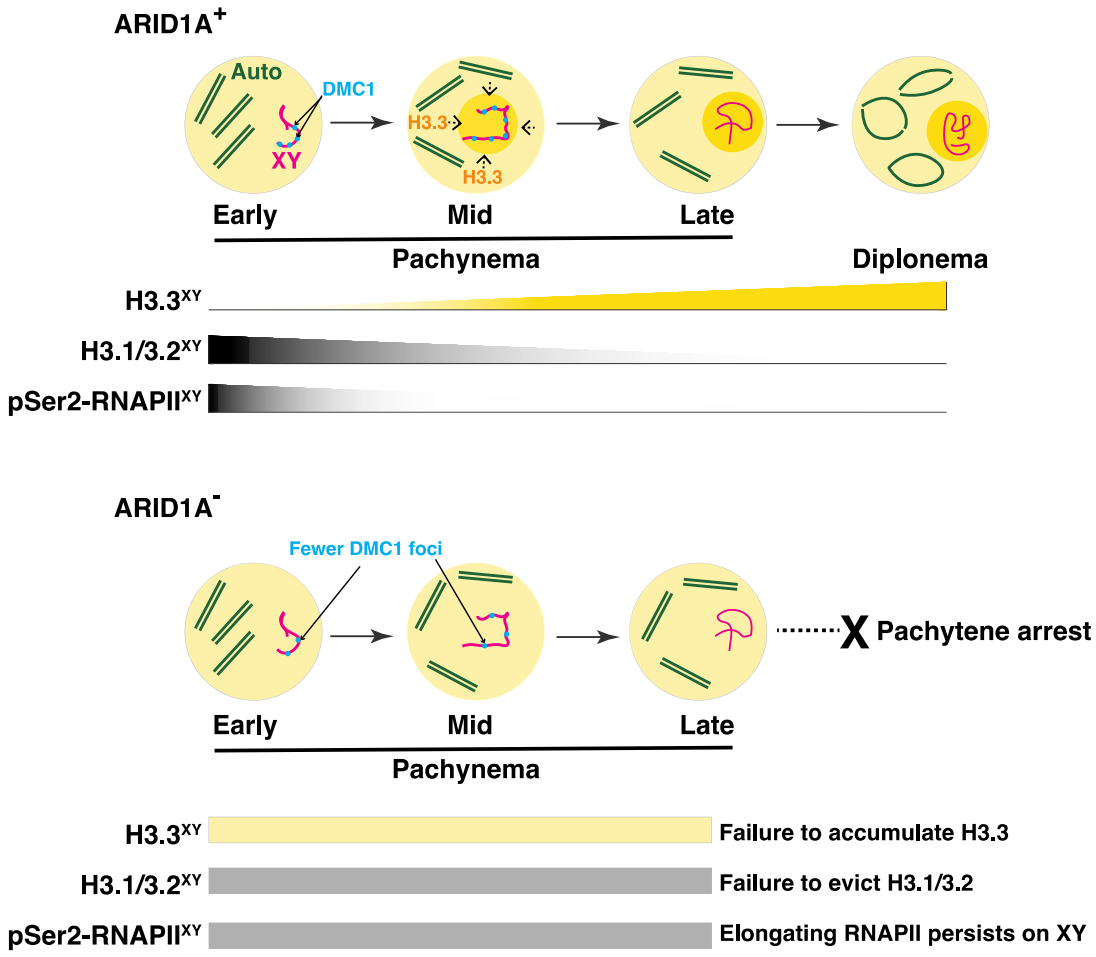

Fig 8. A model describing the role of ARID1A sex-linked chromatin regulation.
During meiosis, the sex chromosomes undergo transcriptional repression at the onset of pachynema. A dramatic change in the composition of sex-linked chromatin accompanies this chromosome-wide repression. From mid to late pachynema, spermatocytes display a hyper-accumulation of the variant histone H3.3 (Ochre shading and gradient) on the sex chromosomes (magenta) relative to autosomes (green). Concomitantly, the levels of the canonical histones H3.1/3.2 and elongating pSer2-RNAPII complex (grey gradients) appear depleted from the sex body by late pachynema. The loss of ARID1A dramatically alters the chromatin composition of the sex body, which features low H3.3 (yellow bar) association at levels indistinguishable from autosomes throughout pachynema. Concomitantly, canonical H3.1/3.2 and pSer2-RNAPII levels (grey bar) on the sex body remain abnormally stable throughout pachynema. These sex-linked chromatin aberrations, along with persistent transcription owing to the association of pSer2-RNAPII with mutant sex body, fail meiotic sex chromosome inactivation (MSCI) and, consequently, pachytene arrest. This defect also coincides with an abnormal loss of DMC1 (blue foci) localization to the unpaired sex chromatids in response to the loss of ARID1A. Therefore, along with transcriptional repression, ARID1A-governed chromatin dynamics appear to influence DNA repair on the sex chromosomes.

445
446
447

448 **Discussion**

449 We previously demonstrated a spermatogenic requirement for the mammalian SWI/SNF
450 complex based on its role in coordinating germline transcription (Menon et al., 2019).
451 Furthermore, we showed that the SWI/SNF PBAF subcomplex activates genes essential for
452 reductional meiosis and gamete formation (Menon et al., 2021). These data highlight that
453 distinct SWI/SNF subcomplexes govern specific meiotic transitions.
454
455 Our current study demonstrates a requirement for the ARID1A-associated BAF (BAF-A)
456 subcomplex for meiotic sex chromosome inactivation (MSCI). It does so by promoting the
457 accumulation of the variant histone H3.3 on the sex chromosomes at the onset of mid-
458 pachynema, coinciding with the eviction of canonical histones H3.1/3.2 and RNA polymerase II
459 from the sex body (Model, Fig. 8). In contrast, when depleted of ARID1A, chromatin accessibility
460 increased along with a deficiency of H3.3 and the continued presence of H3.1/3.2 and pSer2-
461 RNAPII (an elongating form of RNA polymerase II) in the sex body. These data indicate that
462 BAF-A helps define features distinguishing sex chromosomes from autosomes and that the
463 absence of the BAF-A subcomplex during meiosis I results in the failure of MSCI during
464 pachynema.
465
466 Although previous work described the association of H3.3 with the sex body (van der Heijden et
467 al., 2007; Yuen et al., 2014) and its requirement for meiotic repression of sex-linked genes
468 (Fontaine et al., 2022), our study revealed the need for BAF-A in the preferential localization of
469 H3.3 to the sex body relative to autosomes. Interestingly, a similar role for BAF-A in promoting
470 H3.3 incorporation occurs in human endometriotic cells (Reske et al., 2022). In this case, the
471 genomic localization of H3.3 to super-enhancers required ARID1A. Our study describes the
472 ARID1A-dependent localization of H3.3 at a chromosome-wide scale comprised of (i) local
473 enrichment at intergenic loci and (ii) larger domains that resembled spreading much like that of
474 *Xist* during female X chromosome inactivation (XCI) (Chaumeil et al., 2006). X chromosome
475 inactivation (XCI) requires SWI/SNF subunits SMARCA4 and SMARCC1 in female mouse
476 embryonic stem cells (mESC) (Keniry et al., 2022). SMARCC1 promotes XCI by increasing
477 promoter accessibility of the inactive X chromosome (Xi). Interestingly, during MSCI, sex-linked
478 chromatin displays enhanced accessibility (Maezawa et al., 2018b). In contrast, our studies
479 showed that BAF-A limits rather than enhances sex-linked chromatin accessibility. These data
480 highlight a mechanism that checks chromosome-wide relaxation during MSCI. The divergent
481 outcomes of SWI/SNF-governed sex-linked chromatin accessibility during XCI and MSCI

482 probably reflect noticeable sex-specific differences or arise from potentially perturbing distinct
483 SWI/SNF subcomplexes.
484
485 Along with altered chromatin composition and structure, pachytene spermatocytes lacking
486 ARID1A also displayed an abnormal association of pSer2-RNAPII (elongating form) with the sex
487 body. Normally, total transcriptional output peaks towards the end of meiotic prophase-I, even
488 with MSCI coinciding (Alexander et al., 2022; Ernst et al., 2019; MONESI, 1964). The dynamic
489 switching from the paused (pSer5-RNAPII) to the elongating (pSer2-RNAPII) state of RNAPII
490 drives this burst of transcription on autosomes (Alexander et al., 2022). The association of
491 pSer2-RNAPII with the sex chromosomes without ARID1A renders them more autosome-like,
492 underlying the defect in sex-linked gene repression. The BAF-A-governed H3.3 dynamics on the
493 sex chromosomes may limit the switch from the paused to the elongating state of RNAPII. In a
494 human cell culture model, ZMYND11, a known tumor suppressor and reader of Lysine 36
495 trimethylation on H3.3 (H3.3K36me3), suppresses RNAPII elongation (Wen et al., 2014).
496 Whether similar H3.3 readers affect RNAPII pausing during meiosis in mice remains unknown.
497
498 The initiation and maintenance of MSCI are known to be regulated by DNA damage response
499 (DDR) factors, ATR, and MDC1, respectively (Ichijima et al., 2011; Royo et al., 2013; Turner et
500 al., 2004). However, ARID1A deficient pachytene spermatocytes appeared proficient in sex-
501 linked DDR signaling, evidenced by the normal enrichment of ATR, γH2Ax, and MDC1 on the
502 sex body. Therefore, BAF-A-mediated transcriptional repression of the sex chromosomes
503 occurs independently of DDR signaling. Given that the accumulation of ATR and MDC1 on the
504 sex body precedes that of ARID1A, which only manifests late in diplonema, it is reasonable to
505 hypothesize that DDR signaling might recruit BAF-A to the sex chromosomes.
506
507 ARID1A did not appear necessary for sex-linked DNA DSB formation. In contrast, the expected
508 association of DMC1, the meiosis-specific DNA recombinase, with the asynapsed axes of the
509 sex chromosomes do require ARID1A. Interestingly, sex-linked intergenic sites displaying an
510 ARID1A-dependent enrichment of H3.3 appeared depleted for DMC1. Consistent with this
511 antagonism, the loss of ARID1A resulted in the re-distribution of H3.3 to regions normally
512 associated with DMC1. Although only correlative, these data suggest that regions displaying a
513 localized enrichment of H3.3 might be unfavorable for DNA repair. Determining the extent to
514 which a deficiency in BAF-A activity might impede sex-linked DNA repair is challenging. RAD51
515 binding to the sex chromosomes remained stable without ARID1A, suggesting that some sex-

516 linked DNA repair remains. Our studies highlight a model in which BAF-A promotes meiotic
517 progression by facilitating MSCI and DNA repair on the sex chromosomes.
518

519 **Materials and Methods**

520

521 **Generation of *Arid1a* conditional mutant mice**

522 Generation of the *Arid1a*^{tm1Mag}/Mmnc mutant allele was previously described (Chandler et al.,
523 2015). The mice are available through the regional mutant mouse resource and research center
524 (MMRRC; Stock number: 041418-UNC; www.mmrrc.org). *Arid1a* floxed mice
525 (*Arid1a*$^{tm1Mag/}$*Mmnc*) exist on a CD1 genetic background. Crosses with testes-specific *Stra8-Cre*
526 mice (expressed in P3 spermatogonia)(Sadate-Ngatchou et al., 2008) resulted in conditional
527 knockouts. *Arid1a*$^{fl/fl}$; *Stra8- Cre*$^{Tg/0}$ females were crossed to either *Arid1a*$^{fl+}$ or *Arid1a*^{flfl} males to
528 obtain *Arid1a*^{flfl};*Stra8-Cre*$^{Tg/0}$ (*Arid1a*^{cKO}) and either *Arid1a*^{flfl} or *Arid1a*$^{fl+}$ (*Arid1a*^{WT}) males.
529 Haploinsufficiency associated with *Arid1a* negated the possibility of transmitting the Cre through
530 the paternal germline. Genotyping primers: *Arid1a*$^{fl+}$ alleles - (F)- 5' -
531 CTAGGTGGAAGGTAGCTGACTGA -3'; (R) 5' - TACACGGAGTCAGGCTGAGC -3' (PCR
532 product sizes- *fl*: 300 bp; +: 200 bp), and *Stra8-Cre* - (F) 5' -GTGCAAGCTGAACAACAGGA-3',
533 (R) 5' -AGGGACACAGCATTGGAGTC-3' (PCR product size- *Cre*: 150 bp). Mice were housed
534 with a 12hr light cycle (temperature - 20-24° C, humidity - 30-70%). All animal work followed
535 approved UNC Chapel Hill IACUC protocols.

536

537 **Histology**

538 *Arid1a*^{WT} and *Arid1a*^{cKO} testes and cauda epididymites were fixed overnight in Bouins solution
539 (Fisher scientific Ricca chemical; 11-201) at 4° C, followed by dehydration in ethanol series
540 (50%, 70%, and 100%) before embedding in paraffin. The animal histopathology core prepared
541 stained tissue sections (hematoxylin and eosin for cauda epididymites; Periodic acid-Schiff for
542 testes). Staining and morphology determined seminiferous tubule staging (Ahmed and Rooij,
543 2009; Meistrich and Hess, 2013). Summary of staging is provided (Supplementary table 1).

544

545 **Immunofluorescence staining of testis cryosection and spermatocyte spreads**

546 Testes cryosections and spermatocyte spreads from juvenile (P18, P19, and P26) and adult
547 *Arid1a*^{WT} and *Arid1a*^{cKO} mice were examined with indirect immunofluorescence (IF). 8-10 µm
548 thick cryosections of testes were prepared using published methods (Menon et al., 2021).
549 Whole testes were fixed in 10% neutral buffered formalin (NBF) at 4° C for 20 minutes. They
550 were cut in half, followed by 40 minutes of incubation in 10% NBF. Fixed tissues were washed
551 three times (10 minutes per wash) in room temperature (RT) phosphate-buffered saline (PBS)
552 pH7.4. The tissues were then treated with a series of sucrose washes - 10% (30 min), 20% (30

553 min), and 30% (1 hr). Tissues were then incubated at 4° C overnight in a 1:1 ratio of a solution
554 of 30% sucrose/optimum cutting temperature (OCT, Tissue-Tek; 62550-01), followed by
555 embedding in OCT, sectioning, and storage at -80^0 C. Before immunostaining, cryosections
556 were thawed on a heating block at 42^0 C, rehydrated for 10 minutes in PBS, and incubated in
557 10mM citric acid buffer (pH6.0) for 10 minutes at 80-90^0 C (antigen retrieval), during which
558 addition of fresh citrate buffer (80-90 ^{0}C) occurred every 2 minutes, and then allowed to cool for
559 20 minutes. For immunostaining, cryosections were incubated overnight in a humidified
560 chamber with primary antibodies at 4^0 C and then followed by a secondary antibody incubation
561 at RT for 1 hr. Sera were diluted with antibody dilution buffer in PBS (ADB: 3% bovine serum
562 albumin; 10% goat serum; 0.5% Triton-X 100). Two identical blocking steps preceded antibody
563 incubations. These steps involved sequential incubations in (i) PBS, (ii) PBS/0.1% Triton-X 100,
564 and (iii) blocking solution (1:10 dilution of ADB in PBS) for 10 minutes each at RT.
565 Immunostained slides were washed twice in Kodak Photo-Flo 200 (PBS/0.32%), counterstained
566 with DAPI, washed again in PBS/0.32% Photo-Flo 200, and then mounted in Prolong Gold
567 antifade medium (P-36931; Life Technologies).
568
569 Spermatocyte spreads were prepared as previously described (Gray et al., 2020) with minor
570 modifications. Briefly, seminiferous tubules were incubated in hypotonic buffer (30mM Tris
571 pH8.2, 50mM Sucrose, 17 mM Trisodium dihydrate, 5mM EDTA, 0.5mM DTT, 0.1 mM PMSF)
572 for 10-20 minutes on ice. Tubules were minced in 100 mM sucrose (200 µL/testis) until the
573 solution turned turbid. The resulting cell suspension was isolated, avoiding tissue debris, and
574 held on ice. Cells were fixed and spread by dropping 20 µL of cell suspension directly onto glass
575 slides coated with paraformaldehyde solution (1 % Paraformaldehyde; 0.15 % Triton X-100; 625
576 nM Sodium Borate, pH 9.2). Uniform spreading was ensured by tilting the slides along the near
577 and opposite edges. Next, slides were incubated in a humidified chamber for 1 hr, following
578 which they quickly air-dried and then washed two times in PBS/0.32% Photo-Flo 200 and once
579 in H_2O/0.32% Photo-Flo 200. Air-dried slides were immediately processed for immunostaining
580 as described above for cryosections or stored at - 80^0 C. Immunostained spreads were washed
581 2x with PBS/0.32% Photo-Flo 200, counterstained with DAPI, and washed again with Photo-Flo
582 200. Stained spreads were mounted in Prolong Gold antifade medium. The list of antibodies for
583 IF is provided in supplementary table 2. The Leica Dmi8 fluorescent microscope was used to
584 capture images. Z-stacks were deconvoluted using Leica Dmi8 image software (Huygens
585 essentials version 20.04).

586 Fluorescence intensity measurements and object (foci) counting were performed with Fiji
587 (Schindelin et al., 2012). RNAPII (pSer2) IF signal intensities were measured using the method
588 described previously (Menon et al., 2021). Briefly, pixel intensities were recorded from regions
589 of interest (ROI) which include the sex chromosomes (sex body) and an area lacking cells
590 (background fluorescence). Corrected total RNAPII-pSer2 fluorescence (CTRF) was calculated
591 using method previously described (https://theolb.readthedocs.io/en/latest/imaging/measuring-
592 cell-fluorescence-using-imagej.html), where CTRF= Integrated density associated with sex
593 body – (Area of sex body x Mean fluorescence of background).
594 For counting axial DMC1 foci, images were cropped to an area encompassing the sex
595 chromosomes. Cropped images were converted to 8-bit grayscale, and the DMC1 fluorescent
596 channel selected for further processing. An ROI was set, manual thresholding was performed to
597 select DMC foci, and noise (speckles) removed using Fiji median filter tool with a radius set to
598 2.0-4.0. Finally, DMC1 was enumerated with the count particles tool. Statistical significance was
599 calculated using an unpaired student's t-test. Metadata associated with quantification of RNAPII
600 (pSer2) fluorescence and DMC1 foci are provided (Supplementary table 3,4)
601
602 **Preparation of acid-extracted histones and western blotting**
603 Histones from P19 *Arid1a*^{WT} and *Arid1a*^{cKO} spermatogenic cells were acid-extracted using
604 published methods (Shechter et al., 2007). Seminiferous tubules were digested in 1 mL of
605 Enriched Krebs-Ringer Bicarbonate (EKRB) Medium (EKRB salts - 1.2 mM KH_2PO_4, 1.3 mM
606 $CaCl_2$, 119.4 mM NaCl, 4.8 mM KCl, 1.2 mM $MgSO_4$, 11.1 mM Dextrose; 25.2 mM $NaHCO_3$; 1X
607 essential amino acids -Invitrogen, 11130051; 1X non-essential amino acids-Gibco,11140050)
608 supplemented with 0.5 mg/mL collagenase (10 minutes, rotated at 32 ^{o}C). Digested tubules
609 sedimented by gravity for 5 minutes at RT. The supernatant was removed, and tubules were
610 resuspended in 1 mL EKRB medium and then settled for 5 minutes at RT. The sedimented
611 tubules were transferred to 1 mL EKRB medium supplemented with 0.025% trypsin and 4
612 µg/mL DNase-I. The suspension was incubated for 10 minutes on a rotator at 32° C. Digestion
613 was halted with 10% Fetal bovine serum (FBS), and single-cell suspensions were prepared by
614 pipetting the slurry and then filtering it sequentially through 70 µm and 40 µm filters. Cells were
615 pelleted at 600g for 5 minutes, washed once in PBS, and processed for histone extraction.
616 Briefly, cell pellets were resuspended in 1 mL hypotonic lysis buffer (10mM Tris-Cl pH8.0, 1mM
617 KCl, 1.5mM $MgCl_2$, 1mM DTT) and incubated on a rotator at 4° C for 30 minutes. Nuclei were
618 pelleted at 10,000 g for 10 minutes at 4° C. Nuclear pellets were resuspended in 400 µL 0.2N
619 HCl and incubated for 1 hr at 4 ^{o}C, followed by centrifugation at 14,000 g for 10 minutes at 4° C

620 to isolate supernatants containing histones that were precipitated with Trichloroacetic acid
621 (TCA), and then added to the nuclear suspension at a final concentration of 33% and incubated
622 on ice for 30 minutes. Precipitated histones were pelleted at 14,000g for 10 minutes at 4° C and
623 washed two times in 1 mL ice-cold acetone. Finally, washed histones were air-dried at RT for 20
624 minutes and resuspended in 100 µL ddH_2O. For western blots, histones were separated on a 15
625 % SDS-polyacrylamide gel and transferred to PVDF (Polyvinylidene Difluoride) membrane using
626 a semi-dry transfer apparatus (Bio-Rad). Sample loading was assessed by REVERT^{TM} total
627 protein stain (LI-COR, 926-11010). Blots were scanned on a LI-COR Odyssey CLx imager and
628 viewed using Image Studio Version 5.2.5. Antibodies and their corresponding dilutions are listed
629 (Supplementary table 2).
630
631 **Isolation of Pachytene Spermatocytes by the Sta-Put method of Unit Gravity**
632 Pachytene spermatocytes were purified from *Arid1a*^{WT} and *Arid1a*^{cKO} adult testis by the unit
633 gravity sedimentation procedure using a Sta-Put apparatus (Bellvé, 1993; O'Brien, 1993). Testis
634 from at least 12 adult males (>P60) were dissected into EKRB, decapsulated, and digested in
635 0.5mg/ml collagenase for 15 min at 32° C. The resulting tubules were gently washed with EKRB
636 and digested with 0.25mg/ml trypsin supplemented with 4µg/ml DNase for 15 min at 32° C.
637 Following trypsin incubation, additional DNase (4µg/mL) was added to reduce viscosity further.
638 Samples were triturated for 3 minutes with a plastic transfer pipet to fragment flagella, break
639 intercellular bridges between germ cells and further disperse cells into suspension. Trypsin
640 digestion was stopped by adding 0.25mg/mL trypsin inhibitor (Sigma/EPRO, T9003), and cell
641 aggregates were removed by filtration using 40 µm cell strainers. Cells from the flow-through
642 were pelleted at 500g for 5 min at 4° C, resuspended in EKRB + 0.5% BSA, and adjusted to a
643 3.33x10^8 cells/mL density. 10^9 cells from this single-cell suspension were loaded onto a 2-4%
644 linear BSA gradient and allowed to sediment in the Sta-Put apparatus at 4° C. After 2hr and
645 40min of undisturbed sedimentation, 10ml fractions were collected at 45 sec per tube. Fractions
646 were pelleted at 500g for 5 min at 4°C and resuspended in 1ml EKRB + 0.5%BSA. Fractions
647 containing >80% pachytene spermatocytes were identified by light microscopy, pooled, and
648 stored in cryoprotective media (DMEM supplemented with 10%FBS and 20%DMSO) at -80° C
649 pending further analysis.
650
651 **RNA extraction and RT-PCR**
652 Total RNA was isolated in TRIzol^{TM} reagent (Invitrogen, 15596026) from Sta-Put purified
653 fractions enriched for pachytene spermatocytes and round spermatids. The extracted RNA was

654 purified using the Direct-zol RNA kit (Zymo, R2050). cDNA was synthesized using a random
655 primer mix (New England Biolabs, S1330S) and ProtoScript® II reverse transcriptase (New
656 England Biolabs, M0368L). RT-PCR was performed on 1:10 cDNA dilutions using Sso Fast
657 EvaGreen supermix (Bio-Rad, 172-5280) on a thermocycler (BioRad, C1000). Amplicons
658 associated with either floxed or excised *Arid1a* cDNA's were detected using primers: (F)- 5'-
659 TCCAGTAAGGGAGGGCAAGAAGAT -3'; (R) 5'- GTAGTTGGCGTTGGGCAAGGCATTA -3'
660 (PCR product sizes- *fl*: 612 bp; *Δ*: 281 bp)
661
662 **RNA-seq**
663 RNA was extracted and purified in quadruplicate from frozen pellets of *Arid1a*^{WT} and *Arid1a*^{cKO}
664 pachytene spermatocytes obtained bSalmony Sta-Put gravity sedimentation by methods
665 described above. All samples displayed RNA integrity number (RIN) > 7.0 as determined by
666 Agilent Tapestation (High sensitivity RNA screen tape). Sequencing libraries were prepared
667 from 1 µg of total RNA using a Kapa mRNA HyperPrep kit (Roche, KK8580) per the
668 manufacturer's instruction. Libraries were quantified using Qubit™ dsDNA Hs assay kit
669 (Invitrogen, Q32854) pooled at equimolar concentrations, and sequenced on a single lane of the
670 Illumina NovaSeq 6000 S Prime flow cell (50 bp reads, paired-end).
671
672 **RNA-seq data analysis**
673 Quantification of gene expression was done using Salmon (Patro et al., 2017). Transcript counts
674 at the gene level were summarized using tximport (Soneson et al., 2016) and then imported to
675 perform a differential gene expression analysis using DESeq2 (Love et al., 2014). The mouse
676 (mm10) gene/transcript annotations were retrieved using AnotationDbi (Hervé Pagès et al.,
677 2021) and *TxDb.Mus musculus.UCSC.mm10.known gene (Bioconductor Core Team, 2019)*
678 R packages from Bioconductor. Low-count genes (< 10 reads) were pre-filtered and significant
679 differences in counts were called at a false discovery rate (FDR)≤ 0.05. Supplementary Table 5
680 lists differentially expressed genes.
681
682 **CUT&RUN (Cleavage Under Targets and Release Using Nuclease)**
683 CUT&RUN assays were performed on cryopreserved *Arid1a*^{WT} and *Arid1a*^{cKO} pachytene
684 spermatocytes (500,000 cells/genotype) obtained by Sta-Put, using a slightly modified version
685 of previously described methods (Meers et al., 2019; Skene and Henikoff, 2017). For ARID1A,
686 CUT&RUN was performed in triplicates per genotype with two different antibodies. H3.3
687 CUT&RUN was performed in duplicates on *Arid1a*^{WT} and triplicates on *Arid1a*^{cKO} samples.

688 Aliquots of cryopreserved *Arid1a*^{WT} and *Arid1a*^{cKO} pachytene spermatocytes were quickly
689 thawed in a water bath at room temperature (RT), pelleted at 600g for 5 minutes, and washed
690 [wash buffer: 20mM HEPES(Na) pH7.5, 150 mM NaCl, 0.5 mM spermidine, EDTA-free protease
691 inhibitor] three times. Cells were gently resuspended in wash buffer and bound to Concanavalin-
692 A coated magnetic beads (20 µL beads/500,000 cells) by mixing on a rotator for 15 minutes.
693 The bead slurry was separated using a magnet followed by permeabilization in 50 µL antibody
694 buffer (wash buffer + 0.05% Digitonin + 2mM EDTA) per sample in 0.2 mL 8-strip PCR tubes.
695 Primary antibody was added to the samples and incubated on a nutator at 4° C overnight. Cells
696 were then separated using a magnet, washed two times in 200 µL Dig-wash buffer (wash buffer
697 + 0.05% Digitonin), and incubated with a secondary antibody prepared in 50 µL of Dig-wash
698 buffer/sample for 30 minutes on a nutator at 4° C. After antibody incubations, samples were
699 washed twice in 200 µL Dig-wash buffer and then incubated on a nutator at 4° C with 50 µL Dig-
700 wash buffer containing 1000ng/mL Protein A/G Micrococcal Nuclease (pA/G-MNase) for 1 hr.
701 Following this, samples were washed twice in 200 µL Dig-wash buffer, resuspended in 50 µL
702 Dig-wash buffer, cooled down to 0° C, and supplemented with $CaCl_2$ at a final concentration of 2
703 mM to activate MNase. Samples were digested at 0 ^{o}C for 40 minutes. The resulting chromatin
704 fragments were extracted from the bead slurry by incubating in 2X STOP buffer (340 mM NaCl,
705 20mM EDTA, 4mM EGTA, 0.05% Digitonin, 100 µg/mL RNase A) at 37° C for 30 minutes. DNA
706 was purified using ChIP DNA clean and concentrator kit (Zymo, D5205). Libraries were
707 prepared using the Kapa Hyperprep kit (Roche, KK8504), examined for size, and quantified on
708 an Agilent 2100 bioanalyzer using the high-sensitivity DNA kit (Agilent, 5067-4626). The
709 libraries were pooled in equimolar amounts and sequenced on a single lane of the Illumina
710 NovaSeq 6000 S Prime flow cell (50 bp reads, paired-end). Antibody details are listed in
711 Supplementary table 2. The pA/G-MNase (Addgene ID: 123461) used for the CUT&RUN
712 experiments was purified at the Protein Expression and Purification core at UNC Chapel Hill.
713
714
715 **CUT&RUN data analysis**
716 CUT&RUN data analyses were performed as previously described (Menon et al., 2021). Briefly,
717 fastq files were analyzed with fastqc (version 0.11.9), then processed with TrimGalore (version
718 0.6.2, https://www.bioinformatics.babraham.ac.uk/projects/trim_galore/) keeping the --trim-n
719 option. Trimmed reads were aligned to mm10 (mouse) reference genome using bowtie2
720 (Langmead and Salzberg, 2012) parameters: bowtie2 --very-sensitive-local --no-mixed --no-unal
721 --dovetail --no-discordant. Alignments were outputted in BAM format using samtools (Li et al.,

722 2009) and filtered for PCR duplicates using Picard tools, MarkDuplicates
723 (https://broadinstitute.github.io/picard/). Deduplicated BAM files were used to generate bigWig
724 files filtered for ENCODE mm10 blocked regions (Amemiya et al., 2019) with DeepTools,
725 bamCoverage (Ramírez et al., 2016) with the following options: -bs 30 --smoothLength 60 -bl --
726 scaleFactor. The option --scaleFactor was used to normalize for composition bias between
727 CUT&RUN libraries generated from *Arid1a*^{WT} and *Arid1a*^{cKO} pachytene spermatocytes.
728 csaw (Lun and Smyth, 2015) derived normalization factors (nf) were used to calculate the
729 effective library size (library size X nf). The inverse of the effective library size per million was
730 supplied to --scaleFactor to generate normalized bigWig files. Peak calling was performed with
731 MACS2 (version 2.1.2) with options: -f BAMPE --broad --broad-cutoff 0.05 --keep-dup all, on
732 filtered BAM files associated with ARID1A and H3.3 relative to an IgG control previously
733 generated from pachytene enriched populations obtained from P18 testes (Chakraborty and
734 Magnuson, 2022). Peak overlaps across replicates were determined using bedtools intersect
735 (Quinlan and Hall, 2010). Peak calls are provided in supplementary table 6. Peaks were
736 annotated using HOMER (version 4.9.1), annotatePeaks.pl. Replicate bigWig files were
737 averaged using WiggleTools (Zerbino et al., 2014). Averaged bigWig files generated heatmaps
738 with DeepTools, computeMatrix, and plotHeatmap. Data was visualized on Integrative
739 Genomics Viewer (Robinson et al., 2011).
740
741 **ATAC-seq**
742 Cryopreserved aliquots of *Arid1a*^{WT} and *Arid1a*^{cKO} pachytene spermatocytes were processed in
743 quadruplicate for ATAC-seq using the standard Omni-ATAC protocol (Corces et al., 2017) with
744 minor changes. These involved increasing the cell number to 100,000 per replicate, using
745 Diagenode tagmentase (loaded Tn5 transposase, C01070012) and Diagenode 2X tagmentation
746 buffer (C01019043). Libraries were quantified using NEBNext® kit for Illumina® (New England
747 Biolabs, E7630S), pooled at equimolar amounts, and sequenced on a single lane of the Illumina
748 NovaSeq 6000 S Prime flow cell (50 bp reads, paired-end).
749
750 **ATAC-seq data analysis**
751 After analyzing the quality of fastq files with fastqc (version 0.11.9), they were processed with
752 TrimGalore (version 0.6.2), keeping the --trim-n option. Alignments to mm10 reference genome
753 were performed with bowtie2 (Langmead and Salzberg, 2012) parameters: bowtie2 --very-
754 sensitive -X 2000, and outputted in BAM format using samtools. Resultant BAM files were
755 filtered for PCR duplicates using Picard tools, MarkDuplicates, and mitochondrial reads using

samtools view (code: samtools view -h Dedup.bam | grep -v 'chrM' | samtools view -b -h -f 0x2 - | samtools sort > Dedup_noChrM.bam). Filtered BAM files were used to call peaks with MACS2 (parameters: -f BAMPE -n de -q 0.05 --nomodel --nolambda --keep-dup all) and generate normalized bigWig files with DeepTools, bamCoverage (options: -bs 30 --smoothLength 60 -bl --normalized using RPKM). Peak overlaps across replicates were determined using bedtools intersect (Quinlan and Hall, 2010). Peak calls are provided in supplementary table 7. Peak annotation (annotatePeaks.pl) and motif analyses (findMotifsGenome.pl) were performed with HOMER (version 4.9.1). PRDM9 motif frequency near ATAC-seq peaks was determined using HOMER annotatePeaks.pl with options: -size 20000 -hist 10. Replicate bigWig files were averaged using WiggleTools (Zerbino et al., 2014). Averaged bigWig files generated heatmaps with DeepTools, computeMatrix, and plotHeatmap. Data was visualized on Integrative Genomics Viewer (Robinson et al., 2011).

DATA AVAILABILITY:

RNA-seq, CUT&RUN, and ATAC-seq data generated in this study are deposited with GEO (Gene Expression Omnibus) under accession number GSE225612. DMC1 SSDS (GSE35498), RAD51 SSDS (GSE143582), and H3K4me3 ChIP-seq (GSE89502) datasets were previously published (Brick et al., 2012; Hinch et al., 2020; Maezawa et al., 2018a) and are available on GEO.

ACKNOWLEDGEMENTS

We thank Magnuson lab members for their helpful comments on manuscript preparation. Next-generation sequencing was performed at the Duke Center for genomic and computational biology. pA/G-MNase was produced by the Protein Expression and Purification core at the University of North Carolina at Chapel Hill (supported by Cancer Center Support Grant, P30 CA16086). We thank Dr. Atilla Töth (Technishe Universität Dresden) for generously providing the HORMAD1 antibody. This work was supported by National Institutes of Health grants R01GM101974 (T.M).

AUTHOR CONTRIBUTIONS

D.U.M and T.M conceptualized and designed the project. D.U.M. and N.M. carried out experiments. Data curation and validation are done by D.U.M and N.M. The writing was

performed by D.U.M and NM, reviewed and edited by T.M. Project supervision and funding acquisition by T.M.

COMPETING INTERESTS

The authors declare no competing interests.

794 **Figure Legends**

795

796 **Fig S1. ARID1A transcripts detected in pachytene spermatocytes.**

797 scRNA-seq profiles of *Arid1a* and *Arid1b* in adult testes from B6 mice (Ernst et al., 2019). (A)
798 tSNE plot describing the clustering of various spermatogenic stages. LOG2 normalized
799 expression counts of (B,C) *Arid1a* and (D,E) *Arid1b* represented by tSNE plots and bar plots.
800 (B,D) tSNE plots illustrating the first (tSNE1, x-axis) and second dimensions (tSNE2, y-axis) .
801 (C,E) Bar plots describe the gene's mRNA abundance (y-axis) across identified germ cell
802 clusters (x-axis). (A) eP: early pachynema, mP: mid pachynema, lP: late pachynema, MI:
803 Metaphase-I, MII: Metaphase-II, S1-S11: Spermatid stages. Plots generated with shiny app
804 (https://marionilab.cruk.cam.ac.uk/SpermatoShiny)

805

806 **Fig S2. Spermatogenesis appears unperturbed in *Arid1a*^{cKO} males.**

807 Histological examination of (A) PAS-stained seminiferous tubule sections and (B) H&E-stained
808 cauda epididymal sections obtained from 10-week-old *Arid1a*^{WT} *and Arid1a*^{cKO} mice. The
809 micrograph depicts seminiferous tubule staging and scale bars (50 µm). Magnification: 40x.

810

811 **Fig S3. *Arid1a*^{cKO} testes display inefficient *Stra8-Cre* activity.**

812 (A) Schematic (top) illustrating the region of *Arid1a*^{fl} allele spanning exons (ex) 4-8 (grey boxes)
813 along with the location of *loxP* sites (solid magenta arrowheads) and primer annealing sites
814 (blue arrows). (A bottom): analysis of the RT-PCR of *Arid1a* transcripts from STA-PUT purified
815 populations of *Arid1a*^{WT} *and Arid1a*^{cKO} pachytene spermatocytes (left) and round spermatids
816 (right). DNA electrophoresis gels indicate bands corresponding to the fl: floxed and Δ: excised
817 PCR products. *Arid1a*^{WT} and *Arid1a*^{cKO} (B) testes cryosections, and (C) spermatocyte spreads,
818 immunolabelled for ARID1A (magenta), SYCP3 (green), and counterstained for DNA (blue). (B)
819 Scale bar: 20 µm, magnification: 63x, P: Pachytene, D: Diplotene, and M-I: Metaphase-I
820 spermatocytes. (C) Scale bar:15 µm, magnification: 100x.

821

822 **Fig 1. ARID1A associates with the sex body late in meiotic prophase-I.**

823 Representative wild-type pachytene and diplotene spermatocyte spreads immunolabelled for
824 ARID1A (magenta) and SYCP3 (green) and then counterstained for DNA (blue). Scale bar:10
825 µm, magnification: 100x.

826

827 **Table 1. The loss of ARID1A results in a pachytene arrest.**

828 Table outlining the distribution of P23 *Arid1a*^{WT} and *Arid1a*^{cKO} meiotic prophase-I profiles.
829 SYCP3 staining determined meiotic staging. Co-staining of ARID1A identified mutant
830 spermatocytes from internal controls. The total number of spermatocytes scored included 166
831 for *Arida*$^{fl/fl}$ and 124 for *Arid1a*^{cKO}. * denotes *Arid1a*^{cKO} diplotene spermatocytes with partially
832 reduced but not complete loss of ARID1A signal relative to controls.
833
834 **Fig 2. Requirement of ARID1A for the repression of sex-linked genes.**
835 (A) MA plot describing the LOG2-fold-change (LFC, y-axis) in mean expression (x-axis) of
836 genes displaying significant (FDR≤0.05, magenta dots) changes in *Arid1a*^{cKO} relative to
837 *Arid1a*^{WT} pachytene spermatocytes. Dashed blue lines denote 2 LFC. Gray dots (FDR≥0.05)
838 depict non-significant changes in gene expression. (B) Violin plot describing the LOG2-fold-
839 change (LFC, y-axis) in the median chromosome-wide gene expression (x-axis) in *Arid1a*^{cKO}
840 relative to *Arid1a*^{WT} pachytene spermatocytes. The dashed blue line denotes no change in gene
841 expression.
842
843 **Fig S4. Transcription start sites of differentially expressed autosomal and sex-linked**
844 **genes display ARID1A occupancy.**
845 (A-B) Heatmap (bottom) and metaplot (top) displaying the average gene-wide enrichment of
846 ARID1A associated with differentially expressed (A) autosomal and (B) sex-linked genes in
847 *Arid1a*^{WT} and *Arid1a*^{cKO} pachytene spermatocytes. (A-B) The number of RefSeq annotations (n)
848 associated with differentially regulated autosomal and sex-linked genes (rows) is indicated. Up-
849 reg: misexpressed and Dn-reg: misrepressed genes in response to the loss of ARID1A.
850 Average ARID1A CUT&RUN coverage was determined using two antibodies (anti-ARID1A^{Sigma};
851 anti-ARID1A^{CST}) plotted across RefSeq genes ± 3Kb.
852
853 **Fig S5. ARID1A does not influence sex body formation.**
854 (A) *Arid1a*^{WT} and *Arid1a*^{cKO} spermatocyte spreads immunolabelled for ARID1A (magenta) and
855 γH2Ax (green). Scale bar:15 μm, magnification: 100x. (B) Cross section of adult (3-month-old)
856 *Arid1a*^{WT} and *Arid1a*^{cKO} seminiferous tubules immunolabelled for ARID1A (green) and ATR
857 (cyan). Scale bar:15 μm, magnification: 63x. (C) *Arid1a*^{WT} and *Arid1a*^{cKO} pachytene
858 spermatocytes immunolabelled for MDC1 (magenta), SYCP3 (cyan), and ARID1A (green).
859 Scale bar:15 μm, magnification: 100x. (A-B) DNA counterstained with DAPI (blue).
860
861 **Fig 3. ARID1A limits RNA polymerase II (RNAPII) localization to the sex body.**

862 (A) *Arid1a*^{WT} and *Arid1a*^{cKO} pachytene spermatocytes immunolabelled for pSer2-RNAPII
863 (green), SYCP3 (cyan), and counterstained with DAPI (blue). Scale bar:15 µm, magnification:
864 100x. The sex chromosomes (white arrow) and sex body (yellow dashed circle) are labeled. (B)
865 Dot plot describing the corrected total pSer2-RNAPII fluorescence (y-axis) measured from
866 *Arid1a*^{WT} (n = 82) and *Arid1a*^{cKO} (n= 119) pachytene spermatocytes (3 replicates per genotype).
867 Empty diamonds (magenta) represent independent data points. Significance determined by a
868 two-tailed unpaired Student's t-test p values. Data expressed as mean (black dot) ± SEM.
869
870 **Fig 4. ARID1A limits promoter accessibility.**
871 (A) Genomic associations of MACS2 derived ATAC-seq peak calls from *Arid1a*^{WT} and *Arid1a*^{cKO}
872 pachytene spermatocytes. Percent (%) distribution of genomic annotations is indicated. (B-C)
873 Heatmap (bottom) and metaplot (top) displaying the average ATAC-seq signal associated with
874 differentially expressed (B) autosomal and (C) sex-linked genes in *Arid1a*^{WT} and *Arid1a*^{cKO}
875 pachytene spermatocytes. (B-C) The number of RefSeq annotations (n) associated with
876 differentially regulated genes (rows) are indicated. Up-reg: misexpressed, and Dn-reg:
877 misrepressed genes in response to the loss of ARID1A. Average ATAC-seq coverage was
878 plotted across RefSeq genes ± 3Kb.
879
880 **Fig 5. ARID1A influences the chromatin composition of the sex body.**
881 (A-B) *Arid1a*^{WT} and *Arid1a*^{cKO} pachytene spermatocytes immunolabelled for HORMAD1
882 (magenta), (A) ARID1A (cyan) and H3.3 (green), (B) ARID1A (green) and H3.1/3.2 (cyan). (A-
883 B) Proportion (%) of *Arid1a*^{WT} and *Arid1a*^{cKO} early, mid, and late pachytene spermatocytes
884 displaying distinct (A) H3.3, (B) H3.1/3.2 localization patterns with the sex body. For H3.3
885 immunostaining, the total number of *Arid1a*^{WT} pachytene spermatocytes: early = 144, mid= 274,
886 late= 95; *Arid1a*^{cKO} pachytene spermatocytes: early = 43, mid= 86, late= 55, were scored, from
887 3 replicates each. For H3.1/3.2 immunostaining, the total number of *Arid1a*^{WT} pachytene
888 spermatocytes: early = 91, mid= 124, late= 45; *Arid1a*^{cKO} pachytene spermatocytes: early = 22,
889 mid= 116, late= 58, were scored, from 3 replicates each. DNA counterstained with DAPI (blue).
890 The sex chromosomes (yellow arrow) and sex body (yellow dashed circle) are labeled. Scale
891 bar:15 µm, magnification: 100x.
892
893 **Fig S6. ARID1A does not influence the expression or incorporation of H3.3.**
894 (A) Western blots on acid-extracted histones obtained from four independent replicates of P19
895 *Arid1a*^{WT} and *Arid1a*^{cKO} spermatogenic cells, displaying H3.3 abundance. Total histone levels

896 from each sample are displayed. (B) *Arid1a*^{WT} and *Arid1a*^{cKO} pachytene spermatocytes
897 immunolabelled for HORMAD1 (magenta), DAXX (cyan), and ARID1A (green). DNA
898 counterstained with DAPI (blue). The sex chromosomes (yellow arrow) and sex body (yellow
899 dashed circle) are labeled. Scale bar:15 µm, magnification: 100x. (C) *Arid1a*^{WT} and *Arid1a*^{cKO}
900 testis cryosections immunolabelled for ARID1A (magenta) and HIRA (green). DNA
901 counterstained with DAPI (blue). Representative mutant (white arrows) and internal control
902 (yellow arrows) pachytene spermatocytes labeled in *Arid1a*^{cKO} testis cryosection. Scale bar: 15
903 µm, magnification: 63x.
904
905 **Fig S7. ARID1A limits H3.3 occupancy at promoters**
906 (A) Genomic associations of MACS2 H3.3 peak calls from *Arid1a*^{WT} and *Arid1a*^{cKO} pachytene
907 spermatocytes. Percent (%) distribution of genomic annotations is indicated. (B-C) Heatmap
908 (bottom) and metaplot (top) displaying the average H3.3 signal associated with differentially
909 expressed (B) autosomal and (C) sex-linked genes in *Arid1a*^{WT} and *Arid1a*^{cKO} pachytene
910 spermatocytes. (B-C) The number of RefSeq annotations (n) associated with differentially
911 regulated genes (rows) are indicated. Up-reg: misexpressed, and Dn-reg: misrepressed genes
912 in response to the loss of ARID1A. Average H3.3 coverage plotted across RefSeq genes ± 3Kb.
913
914 **Fig S8. Genome browser views of ARID1A governed H3.3 genomic associations.**
915 H3.3 CUT&RUN coverage from *Arid1a*^{WT} (green tracks) and *Arid1a*^{cKO} (Orange tracks)
916 pachytene spermatocytes. Solid red bars and yellow highlights denote H3.3 peak calls (MACS2)
917 from *Arid1a*^{WT} and *Arid1a*^{cKO} pachytene spermatocytes. Vertical viewing limits within
918 parentheses.
919
920
921 **Fig 6. H3.3 displays differential occupancy across ARID1A governed sex-linked open**
922 **chromatin.**
923 (A-B) Heatmaps (bottom) and metaplots (top) displaying average (A) chromatin accessibility
924 (purple heatmap) and H3.3 enrichment (green heatmap) associated with lost, common, and
925 gained ATAC-seq peak calls (MACS2), (B) enrichment of H3.3 at k-means clusters associated
926 with common (C1-C4, left) and gained (G1-G4, right) ATAC-seq peaks, in *Arid1a*^{WT} and
927 *Arid1a*^{cKO} pachytene spermatocytes. (A-B) ATAC-seq and H3.3 coverage plotted over a 5 Kb
928 window centered at ATAC-seq peaks (MACS2). Number of ATAC-seq peak calls (n) associated
929 with each category is indicated.

930

931 **Fig S9. H3.3 occupancy is antagonistic to DMC1 associations in non-homologous sex-**
932 **linked regions.**
933 (A) Genomic associations of common (C1-C4) and gained (G1-G4) k-means clusters in
934 pachytene spermatocytes. Percent (%) distribution of genomic annotations is indicated. (B)
935 Results of PRDM9 motif enrichment analyses at gained (G1 and G3), k-means clusters (top),
936 and plots describing the frequency of PRDM9 motifs (y-axis) spanning a 5 Kb window centered
937 at ATAC-seq peaks (x-axis) associated with gained (middle) and common (bottom) k-means
938 clusters that are either deficient (orange trend line) or enriched (cyan trend line) for H3.3
939 occupancy. Trend lines were generated using generalized additive mode smoothing (gam). 95%
940 confidence interval (gray shading) is indicated. (C-D) Heatmaps displaying testes DMC1 (left)
941 and pachytene spermatocyte associated H3K4me3 (right) enrichment relative to input at k-
942 means clusters associated with (C) gained (G1-G4), and (D) common (C1-C4) ATAC-seq
943 peaks. (C-D) DMC1 and H3K4me3 coverage plotted over a 10 Kb window centered at ATAC-
944 seq peaks (MACS2).
945
946 **Fig 7. ARID1A influences the axial association of DMC1 with the XY during pachynema.**
947 (A) *Arid1a*^{WT} and *Arid1a*^{cKO} pachytene spermatocytes immunolabelled for HORMAD1
948 (magenta), ARID1A (green), DMC1 (cyan), and counterstained with DAPI (blue). Scale bar:15
949 µm, magnification: 100x. A magnified view of the sex chromosomes is indicated (yellow dashed
950 square). (B) Dot plot displaying the number of sex-linked DMC1 foci (y-axis) quantified from
951 *Arid1a*^{WT} (n = 66) and *Arid1a*^{cKO} (ARID1A^{-}, n= 75) pachytene spermatocytes, obtained from 3
952 replicates each. Empty diamonds (magenta) represent independent data points. Significance
953 determined using a two-tailed unpaired Student's t-test p values. Data expressed as mean
954 (black dot) ± SEM.
955
956 **Fig S10. ARID1A does not affect the axial association of RAD51 with the XY during**
957 **pachynema.**
958 (A) Heatmaps displaying testes RAD51 enrichment relative to input at k-means clusters
959 associated with gained (G1-G4, left) and common (C1-C4, right) ATAC-seq peaks. RAD51
960 coverage plotted over a 10 Kb window centered at ATAC-seq peaks (MACS2). (B) *Arid1a*^{WT} and
961 *Arid1a*^{cKO} pachytene spermatocytes immunolabelled for HORMAD1 (magenta), RAD51 (green)
962 and counterstained with DAPI (blue). Scale bar:15 µm, magnification: 100x. Yellow arrows and
963 dashed circles label the sex chromosomes.

964

965 **Fig 8. A model describing the role of ARID1A sex-linked chromatin regulation.**
966 During meiosis, the sex chromosomes undergo transcriptional repression at the onset of
967 pachynema. A dramatic change in the composition of sex-linked chromatin accompanies this
968 chromosome-wide repression. From mid to late pachynema, spermatocytes display a hyper-
969 accumulation of the variant histone H3.3 (Ochre shading and gradient) on the sex
970 chromosomes (magenta) relative to autosomes (green). Concomitantly, the levels of the
971 canonical histones H3.1/3.2 and elongating pSer2-RNAPII complex (grey gradients) appear
972 depleted from the sex body by late pachynema. The loss of ARID1A dramatically alters the
973 chromatin composition of the sex body, which features low H3.3 (yellow bar) association at
974 levels indistinguishable from autosomes throughout pachynema. Concomitantly, canonical
975 H3.1/3.2 and pSer2-RNAPII levels (grey bar) on the sex body remain abnormally stable
976 throughout pachynema. These sex-linked chromatin aberrations, along with persistent
977 transcription owing to the association of pSer2-RNAPII with mutant sex body, fail meiotic sex
978 chromosome inactivation (MSCI) and, consequently, pachytene arrest. This defect also
979 coincides with an abnormal loss of DMC1 (blue foci) localization to the unpaired sex chromatids
980 in response to the loss of ARID1A. Therefore, along with transcriptional repression, ARID1A-
981 governed chromatin dynamics appear to influence DNA repair on the sex chromosomes.
982

983 **References**
984

985 **Ahmed, E. A. and Rooij, D. G. D.** (2009). Meiosis. **558**,.

986 **Alavattam, K. G., Maezawa, S., Andreassen, P. R. and Namekawa, S. H.** (2021). Meiotic sex
987 chromosome inactivation and the XY body: a phase separation hypothesis. *Cell Mol Life*
988 *Sci* **79**, 18.

989 **Alexander, A. K., Rice, E. J., Barshad, G., Zhu, L., Cohen, P. E. and Danko, C. G.** (2022).
990 Meiotic gene transcription programs are mediated by A-MYB and BRDT-dependent
991 RNA polymerase II pause release during mammalian prophase I. *bioRxiv*.

992 **Amemiya, H. M., Kundaje, A. and Boyle, A. P.** (2019). The ENCODE Blacklist: Identification
993 of Problematic Regions of the Genome. *Scientific Reports* **9**, 9354.

994 **Baarends, W. M., Wassenaar, E., van der Laan, R., Hoogerbrugge, J., Sleddens-Linkels, E.,**
995 **Hoeijmakers, J. H. J., de Boer, P. and Grootegoed, J. A.** (2005). Silencing of unpaired
996 chromatin and histone H2A ubiquitination in mammalian meiosis. *Molecular and*
997 *cellular biology* **25**, 1041–1053.

998 **Bellvé, A. R.** (1993). Purification, culture, and fractionation of spermatogenic cells. *Methods*
999 *Enzymol* **225**, 84–113.

1000 **Bioconductor Core Team** (2019). TxDb.Mmusculus.UCSC.mm10.knownGene: Annotation
1001 package for TxDb object(s).

1002 **Brick, K., Smagulova, F., Khil, P., Camerini-Otero, R. D. and Petukhova, G. V.** (2012).
1003 Genetic recombination is directed away from functional genomic elements in mice.
1004 *Nature* **485**, 642–645.

1005 **Chakraborty, P. and Magnuson, T.** (2022). INO80 requires a polycomb subunit to regulate the
1006 establishment of poised chromatin in murine spermatocytes. *Development* **149**,
1007 dev200089.

1008 **Chandler, R. L., Damrauer, J. S., Raab, J. R., Schisler, J. C., Wilkerson, M. D., Didion, J.**
1009 **P., Starmer, J., Serber, D., Yee, D., Xiong, J., et al.** (2015). Coexistent ARID1A–
1010 PIK3CA mutations promote ovarian clear-cell tumorigenesis through pro-tumorigenic
1011 inflammatory cytokine signalling. *Nature Communications* **6**, 6118.

1012 **Chaumeil, J., Le Baccon, P., Wutz, A. and Heard, E.** (2006). A novel role for Xist RNA in the
1013 formation of a repressive nuclear compartment into which genes are recruited when
1014 silenced. *Genes and Development* **20**, 2223–2237.

1015 **Clapier, C. R., Iwasa, J., Cairns, B. R. and Peterson, C. L.** (2017). Mechanisms of action and
1016 regulation of ATP-dependent chromatin-remodelling complexes. *Nature Reviews*
1017 *Molecular Cell Biology*.

1018 **Corces, M. R., Trevino, A. E., Hamilton, E. G., Greenside, P. G., Sinnott-Armstrong, N. A.,**
1019 **Vesuna, S., Satpathy, A. T., Rubin, A. J., Montine, K. S., Wu, B., et al.** (2017). An
1020 improved ATAC-seq protocol reduces background and enables interrogation of frozen
1021 tissues. *Nat Methods* **14**, 959–962.

1022 **ElInati, E., Russell, H. R., Ojarikre, O. A., Sangrithi, M., Hirota, T., de Rooij, D. G.,**
1023 **McKinnon, P. J. and Turner, J. M. A.** (2017). DNA damage response protein TOPBP1
1024 regulates X chromosome silencing in the mammalian germ line. *Proc Natl Acad Sci U S*
1025 *A* **114**, 12536–12541.

1026 **Ernst, C., Eling, N., Martinez-Jimenez, C. P., Marioni, J. C. and Odom, D. T.** (2019). Staged
1027 developmental mapping and X chromosome transcriptional dynamics during mouse
1028 spermatogenesis. *Nature Communications* **10**,.

1029 **Fernandez-Capetillo, O., Mahadevaiah, S. K., Celeste, A., Romanienko, P. J., Camerini-**
1030 **Otero, R. D., Bonner, W. M., Manova, K., Burgoyne, P. and Nussenzweig, A.** (2003).
1031 H2AX is required for chromatin remodeling and inactivation of sex chromosomes in
1032 male mouse meiosis. *Dev Cell* **4**, 497–508.

1033 **Fontaine, E., Papin, C., Martinez, G., Le Gras, S., Nahed, R. A., Héry, P., Buchou, T.,**
1034 **Ouararhni, K., Favier, B., Gautier, T., et al.** (2022). Dual role of histone variant H3.3B
1035 in spermatogenesis: positive regulation of piRNA transcription and implication in X-
1036 chromosome inactivation. *Nucleic Acids Res* **50**, 7350–7366.

1037 **Gray, S., Santiago, E. R., Chappie, J. S. and Cohen, P. E.** (2020). Cyclin N-Terminal
1038 Domain-Containing-1 Coordinates Meiotic Crossover Formation with Cell-Cycle
1039 Progression in a Cyclin-Independent Manner. *Cell Rep* **32**, 107858.

1040 **Handel, M. A.** (2004). The XY body: A specialized meiotic chromatin domain. *Experimental*
1041 *Cell Research* **296**, 57–63.

1042 **Hasegawa, K., Sin, H., Hasegawa, K., Sin, H., Maezawa, S., Broering, T. J., Kartashov, A.**
1043 **V. and Alavattam, K. G.** (2015). SCML2 Establishes the Male Germline Epigenome
1044 through Regulation of Histone H2A Ubiquitination Article SCML2 Establishes the Male
1045 Germline Epigenome through Regulation of Histone H2A Ubiquitination. *Developmental*
1046 *Cell* **32**, 574–588.

1047 **Hervé Pagès, Marc Carlson, Seth Falcon, and Nianhua Li** (2021). AnnotationDbi:
1048 Manipulation of SQLite-based annotations in Bioconductor. **R package version 1.56.2**,.

1049 **Hinch, A. G., Becker, P. W., Li, T., Moralli, D., Zhang, G., Bycroft, C., Green, C., Keeney,**
1050 **S., Shi, Q., Davies, B., et al.** (2020). The Configuration of RPA, RAD51, and DMC1
1051 Binding in Meiosis Reveals the Nature of Critical Recombination Intermediates. *Mol Cell*
1052 **79**, 689-701.e10.

1053 **Hirota, T., Blakeley, P., Sangrithi, M. N., Mahadevaiah, S. K., Encheva, V., Snijders, A. P.,**
1054 **ElInati, E., Ojarikre, O. A., de Rooij, D. G., Niakan, K. K., et al.** (2018). SETDB1

1055 Links the Meiotic DNA Damage Response to Sex Chromosome Silencing in Mice.
1056 *Developmental Cell*.

1057 **Ichijima, Y., Ichijima, M., Lou, Z., Nussenzweig, A., Daniel Camerini-Otero, R., Chen, J.,**
1058 **Andreassen, P. R. and Namekawa, S. H.** (2011). MDC1 directs chromosome-wide
1059 silencing of the sex chromosomes in male germ cells. *Genes and Development* **25**, 959–
1060 971.

1061 **Ichijima, Y., Sin, H.-S. and Namekawa, S. H.** (2012). Sex chromosome inactivation in germ
1062 cells: emerging roles of DNA damage response pathways. *Cell Mol Life Sci* **69**, 2559–
1063 2572.

1064 **Keniry, A., Jansz, N., Gearing, L. J., Wanigasuriya, I., Chen, J., Nefzger, C. M., Hickey, P.**
1065 **F., Gouil, Q., Liu, J., Breslin, K. A., et al.** (2022). BAF complex-mediated chromatin
1066 relaxation is required for establishment of X chromosome inactivation. *Nature*
1067 *Communications* **13**, 1658.

1068 **Khalil, A. M., Boyar, F. Z. and Driscoll, D. J.** (2004). Dynamic histone modifications mark sex
1069 chromosome inactivation and reactivation during mammalian spermatogenesis. *Proc Natl*
1070 *Acad Sci U S A* **101**, 16583–16587.

1071 **Kim, Y., Fedoriw, A. M. and Magnuson, T.** (2012). An essential role for a mammalian
1072 SWI/SNF chromatin-remodeling complex during male meiosis. *Development* **139**, 1133–
1073 1140.

1074 **Langmead, B. and Salzberg, S. L.** (2012). Fast gapped-read alignment with Bowtie 2. *Nature*
1075 *Methods* **9**, 357–359.

1076 **Li, H., Handsaker, B., Wysoker, A., Fennell, T., Ruan, J., Homer, N., Marth, G., Abecasis,**
1077 **G. and Durbin, R.** (2009). The Sequence Alignment/Map format and SAMtools.
1078 *Bioinformatics* **25**, 2078–2079.

1079 **Love, M. I., Huber, W. and Anders, S.** (2014). Moderated estimation of fold change and
1080 dispersion for RNA-seq data with DESeq2. *Genome Biol* **15**, 550.

1081 **Lun, A. T. L. and Smyth, G. K.** (2015). Csaw: A Bioconductor package for differential binding
1082 analysis of ChIP-seq data using sliding windows. *Nucleic Acids Research* **44**, 1–10.

1083 **Maezawa, S., Hasegawa, K., Yukawa, M., Kubo, N. and Sakashita, A.** (2018a). Polycomb
1084 protein SCML2 facilitates H3K27me3 to establish bivalent domains in the male germline
1085 [Genetics]. *Pnas* 3–8.

1086 **Maezawa, S., Yukawa, M., Alavattam, K. G., Barski, A. and Namekawa, S. H.** (2018b).
1087 Dynamic reorganization of open chromatin underlies diverse transcriptomes during
1088 spermatogenesis. *Nucleic Acids Research* **46**, 593–608.

1089 **Manterola, M., Brown, T. M., Oh, M. Y., Garyn, C., Gonzalez, B. J. and Wolgemuth, D. J.**
1090 (2018). BRDT is an essential epigenetic regulator for proper chromatin organization,

1091 silencing of sex chromosomes and crossover formation in male meiosis. *PLoS Genet* **14**,
1092 e1007209.

1093 **Meers, M. P., Bryson, T. D., Henikoff, J. G. and Henikoff, S.** (2019). Improved CUT&RUN
1094 chromatin profiling tools. *eLife*.

1095 **Meistrich, M. L. and Hess, R. A.** (2013). Spermatogenesis. **927**, 299–307.

1096 **Menon, D. U., Shibata, Y., Mu, W. and Magnuson, T.** (2019). Mammalian SWI/SNF
1097 collaborates with a polycomb-associated protein to regulate male germline transcription
1098 in the mouse. *Development* **146**, dev174094.

1099 **Menon, D. U., Kirsanov, O., Geyer, C. B. and Magnuson, T.** (2021). Mammalian SWI/SNF
1100 chromatin remodeler is essential for reductional meiosis in males. *Nature*
1101 *Communications* **12**, 6581.

1102 **Moens, P. B., Chen, D. J., Shen, Z., Kolas, N., Tarsounas, M., Heng, H. H. Q. and**
1103 **Spyropoulos, B.** (1997). Rad51 immunocytology in rat and mouse spermatocytes and
1104 oocytes. *Chromosoma* **106**, 207–215.

1105 **Moens, P. B., Kolas, N. K., Tarsounas, M., Marcon, E., Cohen, P. E. and Spyropoulos, B.**
1106 (2002). The time course and chromosomal localization of recombination-related proteins
1107 at meiosis in the mouse are compatible with models that can resolve the early DNA-DNA
1108 interactions without reciprocal recombination. *J Cell Sci* **115**, 1611–1622.

1109 **MONESI, V.** (1964). RIBONUCLEIC ACID SYNTHESIS DURING MITOSIS AND
1110 MEIOSIS IN THE MOUSE. *The Journal of cell biology*.

1111 **Noe Gonzalez, M., Blears, D. and Svejstrup, J. Q.** (2021). Causes and consequences of RNA
1112 polymerase II stalling during transcript elongation. *Nat Rev Mol Cell Biol* **22**, 3–21.

1113 **O'Brien, D. A.** (1993). Isolation, separation, and short-term culture of spermatogenic cells. In
1114 *Methods in Toxicology*, pp. 246–264. Academic Press, San Diego.

1115 **Patro, R., Duggal, G., Love, M. I., Irizarry, R. A. and Kingsford, C.** (2017). Salmon provides
1116 fast and bias-aware quantification of transcript expression. *Nat Methods* **14**, 417–419.

1117 **Quinlan, A. R. and Hall, I. M.** (2010). BEDTools: A flexible suite of utilities for comparing
1118 genomic features. *Bioinformatics* **26**, 841–842.

1119 **Ramírez, F., Ryan, D. P., Grüning, B., Bhardwaj, V., Kilpert, F., Richter, A. S., Heyne, S.,**
1120 **Dündar, F. and Manke, T.** (2016). deepTools2: a next generation web server for deep-
1121 sequencing data analysis. *Nucleic acids research* **44**, W160–W165.

1122 **Reske, J. J., Wilson, M. R., Armistead, B., Harkins, S., Perez, C., Hrit, J., Adams, M.,**
1123 **Rothbart, S. B., Missmer, S. A., Fazleabas, A. T., et al.** (2022). ARID1A-dependent
1124 maintenance of H3.3 is required for repressive CHD4-ZMYND8 chromatin interactions
1125 at super-enhancers. *BMC Biology* **20**, 209.

1126 **Robinson, J. T., Thorvaldsdóttir, H., Winckler, W., Guttman, M., Lander, E. S., Getz, G.**
1127 **and Mesirov, J. P.** (2011). Integrative genomics viewer. *Nat Biotechnol* **29**, 24–26.

1128 **Rogers, R. S., Inselman, A., Handel, M. A. and Matunis, M. J.** (2004). SUMO modified
1129 proteins localize to the XY body of pachytene spermatocytes. *Chromosoma* **113**, 233–
1130 243.

1131 **Royo, H., Prosser, H., Ruzankina, Y., Mahadevaiah, S. K., Cloutier, J. M., Baumann, M.,**
1132 **Fukuda, T., Höög, C., Tóth, A., de Rooij, D. G., et al.** (2013). ATR acts stage
1133 specifically to regulate multiple aspects of mammalian meiotic silencing. *Genes and*
1134 *Development* **27**, 1484–1494.

1135 **Sadate-Ngatchou, P. I., Payne, C. J., Dearth, A. T. and Braun, R. E.** (2008). Cre recombinase
1136 activity specific to postnatal, premeiotic male germ cells in transgenic mice. *Genesis*
1137 *(New York, N.Y. : 2000)* **46**, 738–742.

1138 **Schimenti, J.** (2005). Synapsis or silence. *Nat Genet* **37**, 11–13.

1139 **Schindelin, J., Arganda-Carreras, I., Frise, E., Kaynig, V., Longair, M., Pietzsch, T.,**
1140 **Preibisch, S., Rueden, C., Saalfeld, S., Schmid, B., et al.** (2012). Fiji: An open-source
1141 platform for biological-image analysis. *Nature Methods*.

1142 **Shechter, D., Dormann, H. L., Allis, C. D. and Hake, S. B.** (2007). Extraction, purification and
1143 analysis of histones. *Nature Protocols* **2**, 1445–1457.

1144 **Skene, P. J. and Henikoff, S.** (2017). An efficient targeted nuclease strategy for high-resolution
1145 mapping of DNA binding sites. *Elife* **6**, e21856.

1146 **Soneson, C., Love, M. I. and Robinson, M. D.** (2016). Differential analyses for RNA-seq:
1147 transcript-level estimates improve gene-level inferences. *F1000Research* **4**, 1521.

1148 **Turner, J. M. a.** (2007). Meiotic sex chromosome inactivation. *Development* **134**, 1823–1831.

1149 **Turner, J. M. A., Aprelikova, O., Xu, X., Wang, R., Kim, S., Chandramouli, G. V. R.,**
1150 **Barrett, J. C., Burgoyne, P. S. and Deng, C. X.** (2004). BRCA1, histone H2AX
1151 phosphorylation, and male meiotic sex chromosome inactivation. *Current Biology* **14**,
1152 2135–2142.

1153 **Turner, J. M. a, Mahadevaiah, S. K., Fernandez-Capetillo, O., Nussenzweig, A., Xu, X.,**
1154 **Deng, C.-X. and Burgoyne, P. S.** (2005). Silencing of unsynapsed meiotic chromosomes
1155 in the mouse. *Nature genetics* **37**, 41–47.

1156 **van der Heijden, G. W., Derijck, A. A. H. A., Pósfai, E., Giele, M., Pelczar, P., Ramos, L.,**
1157 **Wansink, D. G., van der Vlag, J., Peters, A. H. F. M. and de Boer, P.** (2007).
1158 Chromosome-wide nucleosome replacement and H3.3 incorporation during mammalian
1159 meiotic sex chromosome inactivation. *Nature Genetics* **39**, 251–258.

1160 **Wen, H., Li, Y., Xi, Y., Jiang, S., Stratton, S., Peng, D., Tanaka, K., Ren, Y., Xia, Z., Wu, J.,**
1161 **et al.** (2014). ZMYND11 links histone H3.3K36me3 to transcription elongation and
1162 tumour suppression. *Nature* **508**, 263–268.

1163 **Yuen, B. T. K., Bush, K. M., Barrilleaux, B. L., Cotterman, R. and Knoepfler, P. S.** (2014).
1164 Histone H3.3 regulates dynamic chromatin states during spermatogenesis. *Development*
1165 1–12.

1166 **Zerbino, D. R., Johnson, N., Juettemann, T., Wilder, S. P. and Flicek, P.** (2014).
1167 WiggleTools: Parallel processing of large collections of genome-wide datasets for
1168 visualization and statistical analysis. *Bioinformatics*.

1169 **Zhang, Y., Liu, T., Meyer, C. A., Eeckhoute, J., Johnson, D. S., Bernstein, B. E., Nussbaum,**
1170 **C., Myers, R. M., Brown, M., Li, W., et al.** (2008). Model-based analysis of ChIP-Seq
1171 (MACS). *Genome Biology* **9**,.

1172